NASA TM X-39

TECHNICAL MEMORANDUM
X - 39

DYNAMIC LONGITUDINAL AND

DIRECTIONAL STABILITY DERIVATIVES FOR A

45° SWEPTBACK-WING AIRPLANE MODEL AT

TRANSONIC SPEEDS

By Ralph P. Bielat and Harleth G. Wiley

Langley Research Center
Langley Field, Va.

NATIONAL AERONAUTICS AND SPACE ADMINISTRATION
WASHINGTON

August 1959
Declassified August 19, 1960

NATIONAL AERONAUTICS AND SPACE ADMINISTRATION

TECHNICAL MEMORANDUM X-39

DYNAMIC LONGITUDINAL AND DIRECTIONAL STABILITY DERIVATIVES FOR A 45° SWEPTBACK-WING AIRPLANE MODEL AT TRANSONIC SPEEDS

By Ralph P. Bielat and Harleth G. Wiley

SUMMARY

An investigation was made at transonic speeds to determine some of the dynamic stability derivatives of a 45° sweptback-wing airplane model. The model was sting mounted and was rigidly forced to perform a single-degree-of-freedom angular oscillation in pitch or yaw of ±2°. The investigation was made for angles of attack α from -4° to 14° throughout most of the transonic speed range for values of reduced-frequency parameter from 0.015 to 0.040 based on wing mean aerodynamic chord and from 0.04 to 0.14 based on wing span.

The results show that reduced frequency had only a small effect on the damping-in-pitch derivative and the oscillatory longitudinal stability derivative for all Mach numbers M and angles of attack with the exception of the values of damping coefficient near $M = 1.03$ and $\alpha = 8°$ to 14°. In this region, the damping coefficient changed rapidly with reduced frequency and negative values of damping coefficient were measured at low values of reduced frequency. This abrupt variation of pitch damping with reduced frequency was a characteristic of the complete model or wing-body—vertical-tail combination. The damping-in-pitch derivative varied considerably with α and M for the horizontal-tail-on and horizontal-tail-off configurations, and the damping was relatively high at angles of attack corresponding to the onset of pitch-up for both configurations.

The damping-in-yaw derivative was generally independent of reduced frequency and M at $\alpha = -4°$ to 4°. At $\alpha = 8°$ to 14°, the damping derivative increased with an increase in reduced frequency and α for the configurations having the wing, whereas the damping derivative was either independent of or decreased with increase in reduced frequency for the configuration without the wing. The oscillatory directional stability derivative for all configurations generally decreased with an increase in the reduced-frequency parameter, and, in some instances, unstable values were measured for the model configuration with the horizontal tail removed.

INTRODUCTION

Recent design trends in airplanes and missiles have resulted in high-density configurations which have their mass primarily concentrated along the fuselage. As a result, it was believed that some of the dynamic stability derivatives which were previously neglected are important and should be included in the calculations of the motions of the newer configurations. Several low-subsonic investigations have been made of the dynamic stability characteristics of triangular-, swept-, and unswept-wing models (for example, see refs. 1, 2, and 3), and a limited amount of experimental data at supersonic speeds exists for these characteristics (for example, see refs. 4, 5, and 6). At transonic speeds, however, little experimental data exist.

Several methods for investigating dynamic stability in wind tunnels are available such as the free-decay method, self-excitation method, and rigidly forced to oscillate method, but each system has its own limitations. It was believed, however, that the rigidly forced method would be the most suitable to use to investigate dynamic stability at transonic speeds provided that the mechanism for producing reciprocating motion could be contained within the model and that the model could be sting-supported in order to minimize support interference.

A mechanical system for measuring dynamic stability derivatives of models has been designed and constructed for the Langley 8-foot transonic pressure tunnel. In this system, the model was mechanically forced to oscillate in a single degree of freedom at known angular frequency and amplitude while measurements were made of the moment required to sustain the motion. The system allows for a wide range of rigidly controlled frequency and amplitude and is adaptable to almost any model configuration for tests in either pitch or yaw. A somewhat similar system to that described herein for measuring dynamic stability derivatives has been designed for the Langley transonic blowdown tunnel. The results of tests and a description of the mechanism are reported in reference 7.

The present investigation was made in the Langley 8-foot transonic pressure tunnel on a 45° sweptback-wing airplane model. The model was sting mounted and was rigidly forced to perform a single-degree-of-freedom angular oscillation in pitch or yaw of ±2°. The tests were made for angles of attack from -4° to 14° throughout most of the Mach number range from 0.70 to 1.15 for values of reduced-frequency parameter from 0.015 to 0.040 based on wing mean aerodynamic chord and from 0.04 to 0.14 based on wing span. The Reynolds number, based on wing mean aerodynamic chord, varied from 0.99×10^6 to 1.19×10^6.

SYMBOLS

The data presented are referred to the body system of axes, and all moments are referred to the intersection of the oscillation axes which are located at the quarter chord of the wing mean aerodynamic chord. The coefficients and symbols used herein are defined as follows:

b	wing span, ft
C_Y	system damping about Y-axis, ft-lb/radian/sec
C_Z	system damping about Z-axis, ft-lb/radian/sec
$\bar{c}$	wing mean aerodynamic chord, ft
e	base of natural system of logarithms
I_Y	moment of inertia about Y-axis, slug-ft^2
I_Z	moment of inertia about Z-axis, slug-ft^2
$j = \sqrt{-1}$	
K_Y	system spring constant about Y-axis, ft-lb/radian
K_Z	system spring constant about Z-axis, ft-lb/radian
M	Mach number
M_Y	applied moment about Y-axis, ft-lb
M_Z	applied moment about Z-axis, ft-lb
q	angular velocity in pitch, radians/sec
R	Reynolds number based on $\bar{c}$
r	angular velocity in yaw, radians/sec
S	wing area, sq ft
t	time, sec
V	free-stream velocity, ft/sec
Y,Z	lateral and vertical body axes, respectively

α angle of attack of wing chord plane with respect to free-stream direction, deg or radians

β angle of sideslip measured to plane of symmetry and in plane of relative wind, deg or radians

θ phase angle between applied moment and angular displacement, radians

ρ mass density of air, slugs/cu ft

ψ instantaneous displacement angle, radians

ψ_o amplitude of displacement angle, radians

ω angular frequency of oscillation, radians/sec

C_m pitching-moment coefficient, $\dfrac{\text{Pitching moment}}{\frac{1}{2}\rho V^2 S\bar{c}}$

$$C_{m_q} = \frac{\partial C_m}{\partial\left(\frac{q\bar{c}}{2V}\right)}$$

$$C_{m_{\dot{q}}} = \frac{\partial C_m}{\partial\left(\frac{\dot{q}\bar{c}^2}{4V^2}\right)}$$

$$C_{m_\alpha} = \frac{\partial C_m}{\partial \alpha}$$

$$C_{m_{\dot{\alpha}}} = \frac{\partial C_m}{\partial\left(\frac{\dot{\alpha}\bar{c}}{2V}\right)}$$

C_n yawing-moment coefficient, $\dfrac{\text{Yawing moment}}{\frac{1}{2}\rho V^2 Sb}$

$$C_{n_r} = \frac{\partial C_n}{\partial\left(\frac{rb}{2V}\right)}$$

$$C_{n_{\dot{r}}} = \frac{\partial C_n}{\partial\left(\frac{\dot{r}b^2}{4V^2}\right)}$$

$$C_{n_\beta} = \frac{\partial C_n}{\partial \beta}$$

$$C_{n_{\dot{\beta}}} = \frac{\partial C_n}{\partial\left(\frac{\dot{\beta}b}{2V}\right)}$$

Subscripts:

ω data obtained by oscillation tests

aero aerodynamic characteristics

A dot above a symbol denotes differentiation with respect to time.

APPARATUS

For tests, the model configuration was mechanically driven in sinusoidal motion at a constant amplitude of $\pm 2^\circ$ at frequencies varying from 6 to approximately 18.9 cycles per second while measurements were made of the moment required to drive the model.

The mechanism developed for these tests consisted of a model support or carrier which was pivoted about an axis normal to the stream at the upstream end of the sting support (fig. 1). The support and attached model were forced to perform a constant-amplitude, essentially sinusoidal motion about the oscillation axis by a mechanical Scotch yoke and crank arrangement (figs. 2 and 3). The crank was connected by a long drive shaft and magnetic clutch to a 5-horsepower electric motor mounted in the downstream end of the sting. The drive-motor speed was set at various constant values to provide a range of oscillating frequencies. A cantilever spring was mounted between the fixed sting and the oscillating model support (fig. 2). Springs of different stiffnesses provided a range of resonant frequencies within the range of operating frequencies. The cantilever springs were equipped with calibrated strain gages to provide a signal proportional to model displacement. A stiff strain-gage beam, located between the model and the pivot axis, gave a signal proportional to the moment applied to oscillate the model and, because of its location, was uninfluenced by any friction or mechanical play in the system.

Signals from the moment and displacement strain gages were passed through coupled electrical sine-cosine resolvers (fig. 1) which were mounted in the sting fairing forward of the drive motor. The two resolvers were geared to the drive shaft and rotated at the fundamental drive frequency. A 30-pole-signal generator was also attached to the drive shaft to indicate oscillation frequency.

A new sting, which supported the oscillating model and contained the drive shaft, motor, clutch, resolvers, and frequency-signal generator, was constructed for the tests. The sting was equipped with longitudinal stiffeners to provide a sting resonant frequency above the maximum oscillating frequency of the model so that model motion would not excite sting motion. In addition, the sting was rigidly braced to the tunnel walls, floor, and ceiling by preloaded stay cables to restrict any sting motion that might be present (fig. 1). The cables were attached at the sting pivot center to allow an angle-of-attack travel from -4° to 14°.

The oscillating model support and balance assembly was arranged so that the pivot axis could be turned 90° in reference to the model plane of symmetry. Tests could, therefore, be made with the model oscillating in pitch or yaw.

In operation of the system, calibrated outputs of the moment and displacement strain gages were passed through coupled electrical sine-cosine resolvers which rotated at the frequency of oscillation (fig. 1). The resolvers transformed the moment and amplitude functions into orthogonal components which were read on suitably damped direct-current microammeters. From these components, the resultant applied moment and displacement and the phase angle between them were found, and with the known oscillation frequency the aerodynamic damping and oscillatory stability moments were computed. The instrumentation and the block diagram of the electronic circuits used to measure the model displacement and applied moment were similar to that described in reference 7.

The mechanism used in the present tests was designed to provide maximum stiffness of all drive linkages so that the model responded only to the essentially sinusoidal forcing input of the crank and Scotch yoke. The drive shaft was very stiff with the result that twist or wind up between the resolvers and the model was negligible and did not appreciably change over a range of operating frequencies. The resolvers, therefore, could be carefully oriented with the model so that one secondary resolver winding was alined in phase with the model position. Thus, the single output of one displacement winding registered on its meter the full displacement of the model. Similarly, the moment resolver was carefully alined with the model so that one secondary winding was in phase with model displacement and the sum of the moments required to overcome the system spring and inertia forces could be read on one meter. The

other secondary winding of the moment resolver led the model displacement by 90° and was in phase with the model velocity; it, therefore, passed a signal proportional only to model velocity and, thus, registered on the corresponding meter the moment required to overcome the damping.

Because of the rigid sinusoidal input of the Scotch yoke and the controlled phase relationship between the model and resolver axes, the relatively small damping moments on the model system were highly amplified and, thus, resulted in a high accuracy of measurement. Tests could, therefore, be made at speeds other than those at system resonance with considerable accuracy.

The static pitching and yawing moments were measured with the displacement beam removed and the drive shaft and model locked at a displacement of 0°.

MODEL

Two-view drawings showing the physical characteristics of the model used in this investigation are presented in figure 4. Lightweight materials were used in the construction of the model; and the center of gravity of the model, although not coincident, was near the axis of rotation to reduce the moment-of-inertia effects insofar as possible. The model had an aluminum wing with 45° sweepback at the quarter chord, an aspect ratio of 4.0, a taper ratio of 0.2, and an NACA 65A005 airfoil section parallel to the plane of symmetry. The wing was mounted on the fuselage center line with an angle of incidence of 0° and had no twist or dihedral. The horizontal tail was made of aluminum and had 45° sweepback at the quarter chord, an aspect ratio of 3.5, a taper ratio of 0.4, and an NACA 65A005 airfoil section parallel to the plane of symmetry. The horizontal tail was mounted on the fuselage center line with an angle of incidence of 0°. The vertical tail was made of aluminum and had 45° sweepback at the quarter chord, an aspect ratio of 1.23, a taper ratio of 0.4, and an NACA 65A005 airfoil section parallel to the stream. The fuselage, which was made of magnesium, had an ogive nose and a cylindrical afterbody and had a fineness ratio of 9.84. Fuselage coordinates are given in figure 4. The axes of pitch and yaw rotation passed through the intersection of the fuselage longitudinal center line and the quarter chord of the wing mean aerodynamic chord. A photograph showing the model and the method of supporting it in the wind tunnel is presented in figure 5.

TESTS

The tests were conducted in the Langley 8-foot transonic pressure tunnel, which is rectangular in cross section. The upper and lower walls

of the test section are slotted to permit continuous operation through the transonic speed range. The tests were made through a Mach number range from 0.70 to 1.15. All data presented from this tunnel are essentially free of wall-reflected disturbances. The tests were performed at approximately one-half atmospheric stagnation pressure and at a dew-point temperature such that the air flow was free of condensation shocks. For the present tests, the Reynolds number, based on wing mean aerodynamic chord, varied from 0.99×10^6 to 1.19×10^6 (fig. 6).

Measurements were made of the damping-in-pitch parameter $C_{m_{q,\omega}} + C_{m_{\dot{\alpha},\omega}}$, the oscillatory longitudinal stability derivative $C_{m_{\alpha,\omega}} - \left(\frac{\omega\bar{c}}{2V}\right)^2 C_{m_{\dot{q},\omega}}$, the damping-in-yaw parameter $C_{n_{r,\omega}} - C_{n_{\dot{\beta},\omega}} \cos\alpha$, and the oscillatory directional stability derivative $C_{n_{\beta,\omega}} \cos\alpha + \left(\frac{\omega b}{2V}\right)^2 C_{n_{\dot{r},\omega}}$ at angles of attack from -4° to 14° throughout most of the Mach number range. The reduced-frequency parameter in pitch $\omega\bar{c}/2V$ varied from 0.015 to 0.040, the reduced-frequency parameter in yaw $\omega b/2V$ varied from 0.04 to 0.14, and the maximum amplitude of pitch and yaw oscillation was $\pm 2^\circ$ for the tests. Measurements of the static pitching moment and yawing moment were made at angles of attack from -4° to 14° throughout most of the Mach number range. The static yawing moments were measured for angles of sideslip of $\pm 2^\circ$.

All tests were conducted with fixed transition on the model according to the methods described in reference 8. The transition was fixed by applying 1/8-inch-wide strips of No. 60 carborundum grains around the body 1 inch back from the nose and to both the upper and lower surfaces of the wing at the 10-percent-chord location. Transition on the tail surfaces was fixed by spraying both sides of these surfaces with 1/8-inch-wide strips of an adhesive liquid at the 10-percent-chord location.

REDUCTION OF OSCILLATION-TEST DATA

A complete discussion of the principles of measuring dynamic stability derivatives by the forced-oscillation technique and of the methods involved are presented in appendix A of reference 7; therefore, only a brief description of the expressions for the oscillatory derivatives is given herein. In this method of measuring dynamic stability derivatives by the force-driven technique, the model is rigidly forced to perform a single-degree-of-freedom oscillation while measurements are made of the model motion and of the moment required to sustain the motion. For example, the model, when oscillating in yaw only, is a simple single-degree-of-freedom mechanical system whose characteristics are related

by the differential equation

$$I_Z\ddot{\psi} + C_Z\dot{\psi} + K_Z\psi = M_Z e^{j(\omega t+\theta)} \tag{1}$$

The equation of motion is

$$\left(-I_Z\omega^2 + jC_Z\omega + K_Z\right)\psi_o = M_Z e^{j\omega t} \tag{2}$$

The vector diagram of equation (2) is shown in the following sketch with the real axis alined with the displacement vector:

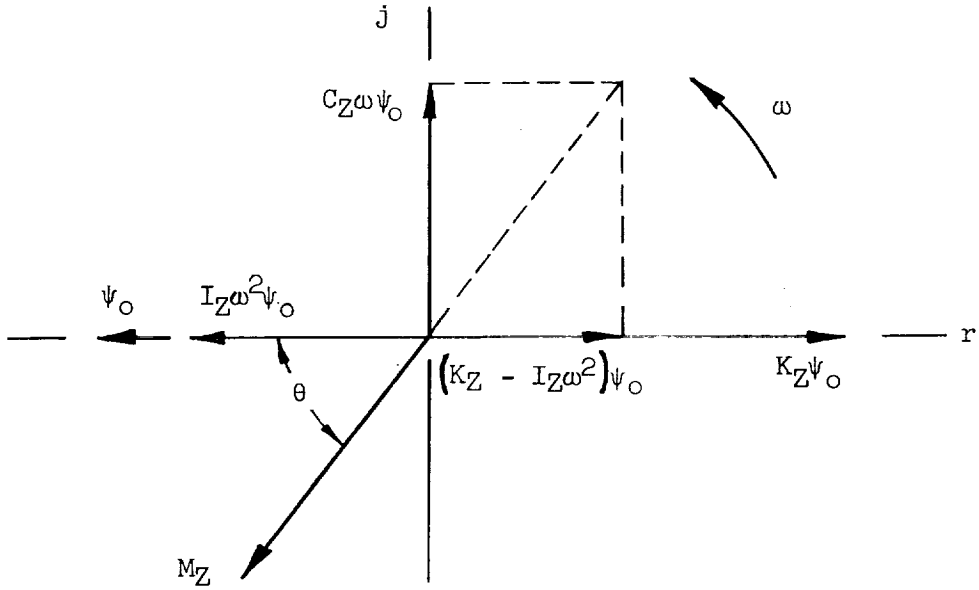

For equilibrium of the vector diagram, the imaginary components may be related by

$$C_Z\omega\psi_o = M_Z \sin\theta$$

and the total system damping is

$$C_Z = \frac{M_Z \sin\theta}{\omega\psi_o} \tag{3}$$

Similarly, the real components may be related by

$$K_Z\psi_o - I_Z\omega^2\psi_o = M_Z \cos \theta$$

and the total system spring constant is

$$K_Z = \frac{M_Z \cos \theta}{\psi_o} + I_Z\omega^2 \tag{4}$$

The aerodynamic damping and aerodynamic spring constant or oscillatory directional stability were determined by subtracting the combined mechanical and viscous forces (tare characteristics) of the system from the total system characteristics measured in the wind tunnel as follows:

$$C_{Z,aero} = \left[\left(\frac{M_Z \sin \theta}{\psi_o\omega}\right)_{wind\ on} - \left(\frac{M_Z \sin \theta}{\psi_o\omega}\right)_{wind\ off}\right] \tag{5}$$

$$K_{Z,\ aero} = \left[\left(\frac{M_Z \cos \theta}{\psi_o} + I_Z\omega^2\right)_{wind\ on} - \left(\frac{M_Z \cos \theta}{\psi_o} + I_Z\omega^2\right)_{wind\ off}\right] \tag{6}$$

The tare or wind-off characteristics were generally measured at atmospheric pressure and, in some instances, the tares were also determined at a pressure equal to one-half atmospheric pressure. It was found from these measurements that the amount of viscous damping present was very small and also that the combined mechanical and viscous tare was a small part of the total aerodynamic damping measured. These aerodynamic characteristics were reduced to coefficient form in the manner described in reference 2 so that the damping coefficient is

$$C_{n_r} - C_{n_{\dot\beta}} \cos \alpha = \frac{-C_{Z,aero}(2V)}{qSb^2} \tag{7}$$

and the oscillatory directional stability coefficient is

$$C_{n_\beta} \cos \alpha + \left(\frac{\omega b}{2V}\right)^2 C_{n_{\dot r}} = \frac{K_{Z,aero}}{qSb} \tag{8}$$

The expression "cos α" appears in equations (7) and (8) because the coefficients are expressed in the body-axis system.

In a similar manner, the damping in pitch and the oscillatory longitudinal stability were determined as follows:

$$C_{Y,aero} = \left[\left(\frac{M_Y \sin\theta}{\psi_o \omega}\right)_{wind\ on} - \left(\frac{M_Y \sin\theta}{\psi_o \omega}\right)_{wind\ off}\right] \quad (9)$$

$$K_{Y,aero} = \left[\left(\frac{M_Y \cos\theta}{\psi_o} + I_Y\omega^2\right)_{wind\ on} - \left(\frac{M_Y \cos\theta}{\psi_o} + I_Y\omega^2\right)_{wind\ off}\right] \quad (10)$$

When reduced to coefficient form, the damping coefficient is

$$C_{m_q} + C_{m_{\dot{\alpha}}} = \frac{-C_{Y,aero}(2V)}{qS\bar{c}^2} \quad (11)$$

and the oscillatory longitudinal stability coefficient is

$$C_{m_\alpha} - \left(\frac{\omega\bar{c}}{2V}\right)^2 C_{m_{\dot{q}}} = \frac{-K_{Y,aero}}{qS\bar{c}} \quad (12)$$

RESULTS AND DISCUSSION

Presentation of Data

In the discussion of the results that follows, the complete model refers to the configuration having the wing, body, and horizontal and vertical tails.

The static-pitching-moment data are shown in figure 7. The longitudinal-oscillation test data are shown for $C_{m_{q,\omega}} + C_{m_{\dot{\alpha},\omega}}$ in figures 8 to 12 and for $C_{m_{\alpha,\omega}} - \left(\frac{\omega\bar{c}}{2V}\right)^2 C_{m_{\dot{q},\omega}}$ in figures 13 to 17. The

directional-oscillation test data for $C_{n_{r,\omega}} - C_{n_{\dot{\beta},\omega}} \cos \alpha$ are presented in figures 18 to 26 and for $C_{n_{\beta,\omega}} \cos \alpha + \left(\frac{\omega b}{2V}\right)^2 C_{n_{\dot{r},\omega}}$ in figures 27 to 35.

The static-pitching-moment data plotted against angle of attack for the complete model and for the wing-body—vertical-tail configuration shown in figure 7 are included herein primarily to relate the pitching-moment characteristics of the model to the angle of attack. It will be noted that a pitch-up tendency exists above an angle of attack of about 8° for most Mach numbers for both the complete model and the wing-body—vertical-tail configuration.

Longitudinal Dynamic Stability

Damping-in-pitch derivative $C_{m_{q,\omega}} + C_{m_{\dot{\alpha},\omega}}$.- In general, the results shown in figures 8 and 9 indicate only small variations of the damping-in-pitch derivative $C_{m_{q,\omega}} + C_{m_{\dot{\alpha},\omega}}$ with reduced frequency $\omega\bar{c}/2V$ for all Mach numbers and angles of attack with the exception of values of damping coefficient near $M = 1.03$ and at $\alpha = 8^\circ$ to 14°. In this region, it will be noted that the damping coefficient changes very rapidly with reduced frequency and values of zero or negative damping (positive damping coefficients) were measured at the low values of $\omega\bar{c}/2V$. These changes apparently result from the time-lag effects of the shock-induced separation over the wing since similar characteristics were observed for the model both with and without horizontal tail (figs. 8 and 9). The variation of $C_{m_{q,\omega}} + C_{m_{\dot{\alpha},\omega}}$ with angle of attack at various values of $\omega\bar{c}/2V$ for the complete model and the wing-body—vertical-tail configuration is shown in figures 10 and 11, respectively, and the variation of the damping-in-pitch coefficient with Mach number for the complete model and wing-body—vertical-tail configuration plotted for constant values of reduced frequency $\omega\bar{c}/2V$ of 0.016 and 0.024 is shown in figure 12. The damping-in-pitch coefficient varied considerably with angle of attack and Mach number for the horizontal-tail-on and horizontal-tail-off configurations. The damping is relatively high at angles of attack corresponding to the onset of pitch-up for both model configurations. (Compare figs. 10 and 11 with fig. 7.) Although the level of pitch damping was higher for the horizontal-tail-on configuration than for the horizontal-tail-off configuration, the trends of pitch damping with Mach number and angle of attack are very similar for both configurations and, thus, indicate that the wing and not the horizontal tail is responsible for the nonlinear trends.

Longitudinal stability derivative $C_{m_{\alpha,\omega}} - \left(\frac{\omega\bar{c}}{2V}\right)^2 C_{m_{\dot{q},\omega}}$.- The values of the longitudinal stability derivative $C_{m_{\alpha,\omega}} - \left(\frac{\omega\bar{c}}{2V}\right)^2 C_{m_{\dot{q},\omega}}$ obtained during the forced-oscillation tests are presented in figures 13 and 14. Static-longitudinal-stability data ($\omega\bar{c}/2V = 0$) from figure 7 have also been plotted in these figures and in figures 15 and 16 for comparison with the oscillation results. Generally, the reduced-frequency parameter $\omega\bar{c}/2V$ had little effect on the oscillatory longitudinal stability derivative $C_{m_{\alpha,\omega}} - \left(\frac{\omega\bar{c}}{2V}\right)^2 C_{m_{\dot{q},\omega}}$ for all Mach numbers and angles of attack, and the oscillatory derivatives at low values of $\omega\bar{c}/2V$ differed little from the static derivatives. A reduction in the oscillatory longitudinal stability derivative can be noted at angles of attack near 8° (figs. 15 and 16) which corresponds to the angle of attack where static pitch-up occurs (fig. 7).

The oscillatory longitudinal stability derivative generally increased with Mach number for angles of attack up to 8° (fig. 17). For the higher angles of attack ($\alpha = 12^\circ$ and 14°), the longitudinal stability derivative decreased with increase in Mach number above about $M = 0.95$.

Directional Dynamic Stability

Damping-in-yaw derivative $C_{n_{r,\omega}} - C_{n_{\dot{\beta},\omega}} \cos\alpha$.- The damping-in-yaw derivative $C_{n_{r,\omega}} - C_{n_{\dot{\beta},\omega}} \cos\alpha$ was generally independent of reduced frequency at angles of attack from -4° to 4° for all Mach numbers (figs. 18 to 21). For the angles of attack from 8° to 14°, the damping in yaw increased with $\omega b/2V$ for all configurations having the wing (figs. 18, 19, and 20), whereas the damping derivative was either independent of or decreased with an increase in $\omega b/2V$ for the configuration having a body, horizontal tail, and vertical tail (fig. 21).

The basic data from figures 18 to 21 have been cross plotted in figures 22 to 25 to illustrate more clearly the variation of $C_{n_{r,\omega}} - C_{n_{\dot{\beta},\omega}} \cos\alpha$ with angle of attack for various values of $\omega b/2V$ and Mach number. The results of figures 22 to 24 show that the damping-in-yaw derivative was independent of or decreased with angle of attack up to about 8° and then increased with a further increase in angle of attack up to 14° which was the maximum value of the present tests. Similar increases in the damping-in-yaw derivative have been noted in low-speed tests for swept wings with the exception that the increases in $C_{n_{r,\omega}} - C_{n_{\dot{\beta},\omega}} \cos\alpha$ occurred at angles of attack above about 14°.

(See refs. 1, 2, and 3.) The increases in the damping-in-yaw derivative above 14° were attributed in the low-speed tests to flow separation over the wings. Some tests were made herein with the wings removed from the model and the results, which are presented in figure 25, also indicate that the increases in the damping-in-yaw derivative were due to the presence of the wing.

The variation of the damping-in-yaw derivative $C_{n_{r,\omega}} - C_{n_{\dot{\beta},\omega}} \cos \alpha$ with Mach number for various model configurations plotted for a constant value of reduced frequency $\omega b/2V$ of 0.075 is shown in figure 26. The data indicate that the damping-in-yaw derivative was stable throughout the Mach number range and, in general, the variations with Mach number were small for angles of attack up to 12°. It will also be noted that the vertical tail produced the greatest contribution to the total damping-in-yaw derivative.

Directional stability derivative $C_{n_{\beta,\omega}} \cos \alpha + \left(\frac{\omega b}{2V}\right)^2 C_{n_{\dot{r},\omega}}$.- The values of the directional stability derivative $C_{n_{\beta,\omega}} \cos \alpha + \left(\frac{\omega b}{2V}\right)^2 C_{n_{\dot{r},\omega}}$ obtained during the forced-oscillation tests are presented in figures 27 to 30. Static-directional-stability data ($\omega b/2V = 0$) for the complete model, for the wing-body—horizontal-tail configuration, and for the configuration having a body, horizontal tail, and vertical tail have been plotted in figures 27, 28, and 30, respectively, for comparison with the oscillation results. For very low values of reduced frequency where $\omega b/2V$ approaches zero, the values of $C_{n_{\beta,\omega}} \cos \alpha + \left(\frac{\omega b}{2V}\right)^2 C_{n_{\dot{r},\omega}}$ measured in the oscillation tests tend to approach the values of C_{n_β} measured in the static-force tests. Increasing the reduced-frequency parameter $\omega b/2V$ generally decreased the directional stability derivative for all configurations; and in some instances, with the vertical tail installed but the horizontal tail removed, unstable values of $C_{n_{\beta,\omega}} \cos \alpha + \left(\frac{\omega b}{2V}\right)^2 C_{n_{\dot{r},\omega}}$ were measured (fig. 29). This result was most likely due to the decreased vertical-tail effectiveness resulting from the removed favorable end-plate effect of the horizontal tail.

A slight decrease in directional stability was indicated with increase in angle of attack for all the configurations having the vertical tail (figs. 31, 33, and 34) and became greater at the highest test Mach number. With the vertical tail off (fig. 32), the configuration was directionally unstable and was uninfluenced by angle-of-attack changes.

Figure 35 shows the variation of $C_{n_{\beta,\omega}} \cos \alpha + \left(\frac{\omega b}{2V}\right)^2 C_{n_{\dot{r},\omega}}$ with Mach number for various angles of attack and model configurations plotted for a constant value of $\omega b/2V$ of 0.075. In general, the directional stability derivative showed only a small variation with Mach number throughout the angle-of-attack range.

SUMMARY OF RESULTS

The results of a wind-tunnel investigation at transonic speeds to determine some of the dynamic stability derivatives in pitch and in yaw of a 45° sweptback-wing airplane model oscillating at ±2° amplitude are summarized as follows:

1. Reduced frequency had only a small effect on the damping-in-pitch derivative for all Mach numbers and angles of attack with the exception of the values of damping coefficient near a Mach number of 1.03 and angles of attack from 8° to 14°. In this region, the damping coefficient changed very rapidly with reduced frequency, and zero or negative values of damping coefficient were measured at the low values of reduced frequency. This abrupt variation of damping in pitch with reduced frequency was a characteristic of the complete model or wing-body—vertical-tail combination.

2. The damping-in-pitch coefficient varied considerably with angle of attack and Mach number for the horizontal-tail-on and horizontal-tail-off configurations, and the damping was relatively high at angles of attack corresponding to the onset of pitch-up for both model configurations. Although the level of pitch damping was higher for the horizontal-tail-on configuration than for the horizontal-tail-off configuration, the trends of pitch damping with Mach number and angle of attack were very similar for both configurations and, thus, indicated that the wing and not the horizontal tail was responsible for the nonlinear trends.

3. Reduced frequency had little effect on the oscillatory longitudinal stability derivative for all Mach numbers and angles of attack. At low values of reduced frequency approaching zero, the oscillatory longitudinal stability derivative approached the steady-state values of longitudinal stability measured in the static-force tests.

4. The damping-in-yaw derivative was generally independent of reduced frequency and Mach number in the low angle-of-attack range (-4° to 4°). At high angles of attack (8° to 14°), the damping derivative increased with an increase in reduced frequency and angle of attack for the configurations having the wing, whereas the damping

derivative was either independent of or decreased with increase in reduced frequency for the configuration without the wing.

5. The oscillatory directional stability derivative for all configurations generally decreased with an increase in reduced frequency and, in some instances, unstable values of the directional stability derivative were measured for the model configuration with the horizontal tail removed.

6. A slight decrease in directional stability was indicated with increase in angle of attack for all the configurations with the vertical tail installed and became greater at the highest test Mach number. With the vertical tail off, the configuration was directionally unstable and was uninfluenced by changes in angle of attack or Mach number.

7. At very low values of reduced frequency, the oscillatory directional stability derivative tended to approach the steady-state values of directional stability measured in the static-force tests.

Langley Research Center,
National Aeronautics and Space Administration,
Langley Field, Va., April 8, 1959.

REFERENCES

1. Fisher, Lewis R.: Experimental Determination of the Effects of Frequency and Amplitude on the Lateral Stability Derivatives for a Delta, a Swept, and an Unswept Wing Oscillating in Yaw. NACA Rep. 1357, 1958. (Supersedes NACA RM L56A19.)

2. Campbell, John P., Johnson, Joseph L., Jr., and Hewes, Donald E.: Low-Speed Study of the Effect of Frequency on the Stability Derivatives of Wings Oscillating in Yaw With Particular Reference to High Angle-of-Attack Conditions. NACA RM L55H05, 1955.

3. Letko, William, and Fletcher, Herman S.: Effects of Frequency and Amplitude on the Yawing Derivatives of Triangular, Swept, and Unswept Wings and of a Triangular-Wing—Fuselage Combination With and Without a Triangular Tail Performing Sinusoidal Yawing Oscillations. NACA TN 4390, 1958.

4. Beam, Benjamin H.: A Wind-Tunnel Test Technique for Measuring the Dynamic Rotary Stability Derivatives at Subsonic and Supersonic Speeds. NACA Rep. 1258, 1956. (Supersedes NACA TN 3347.)

5. Lampkin, Bedford A., and Tunnell, Phillips J.: Static and Dynamic-Rotary Stability Derivatives of an Airplane Model With an Unswept Wing and a High Horizontal Tail at Mach Numbers of 2.5, 3.0, and 3.5. NACA RM A58F17, 1958.

6. Moore, John A.: Experimental Determination of Damping in Pitch of Swept and Delta Wings at Supersonic Mach Numbers. NACA RM L57G10a, 1957.

7. Braslow, Albert L., Wiley, Harleth G., and Lee, Cullen Q.: Dynamic Directional Stability Derivatives for a 45° Swept-Wing—Vertical-Tail Airplane Model At Transonic Speeds and Angles of Attack, With a Description of the Mechanism and Instrumentation Employed. NACA RM L58A28, 1958.

8. Braslow, Albert L., and Knox, Eugene C.: Simplified Method for Determination of Critical Height of Distributed Roughness Particles for Boundary-Layer Transition at Mach Numbers From 0 to 5. NACA TN 4363, 1958.

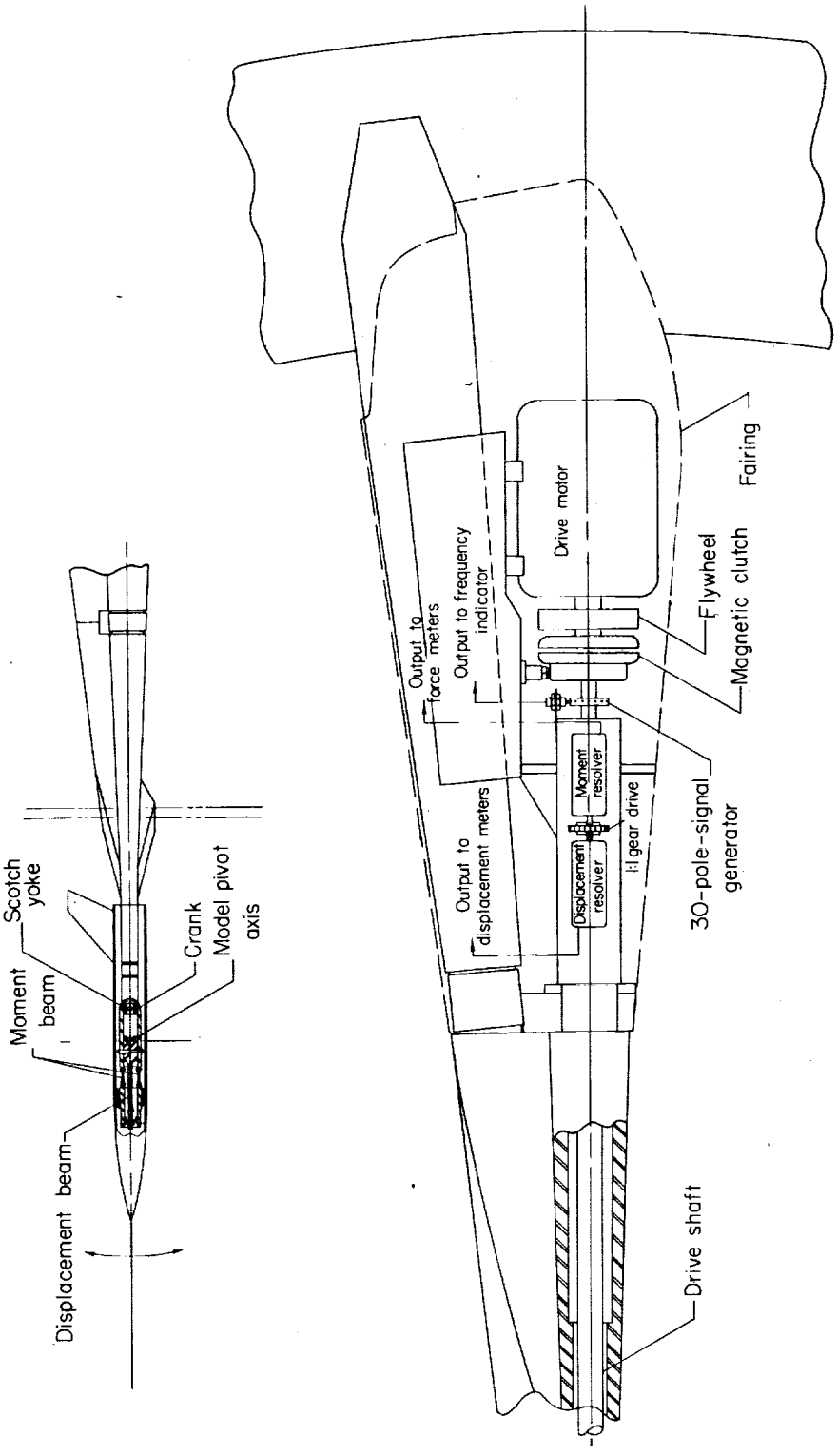

Figure 1.- Schematic view of model and driving-system components.

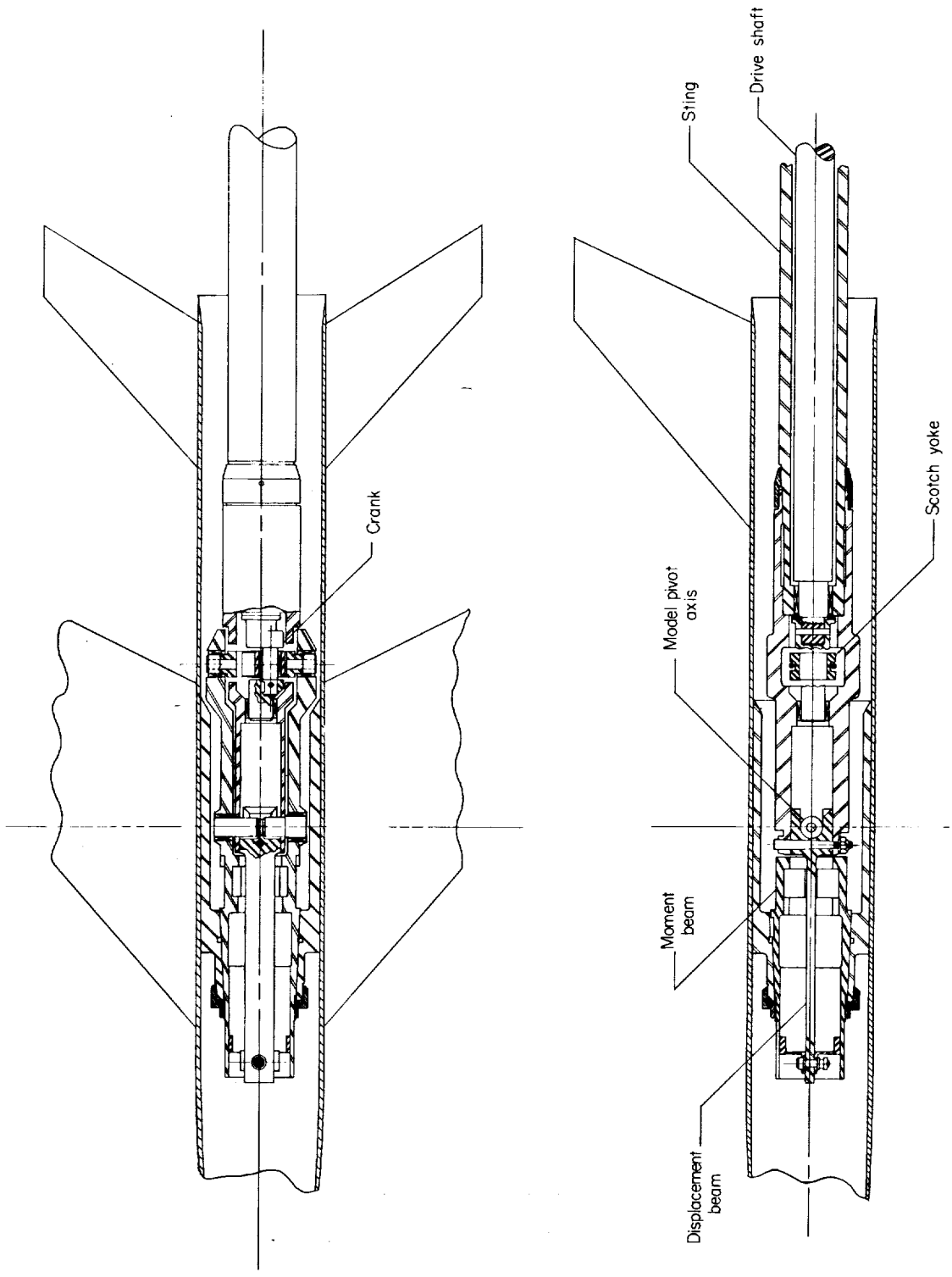

Figure 2.- Details of oscillating mechanism.

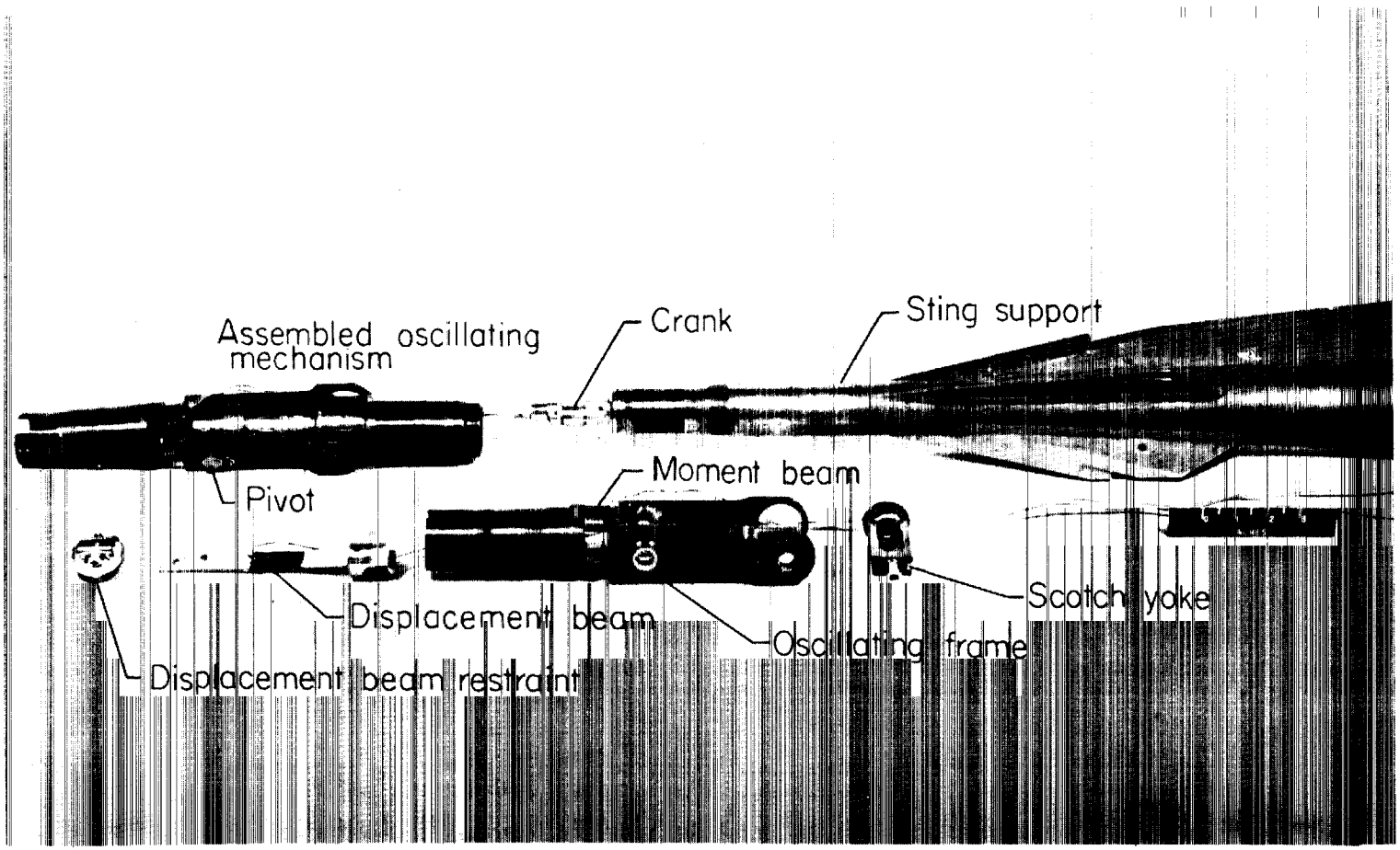

Figure 3.- Exploded view of oscillating mechanism. L-58-2085.2

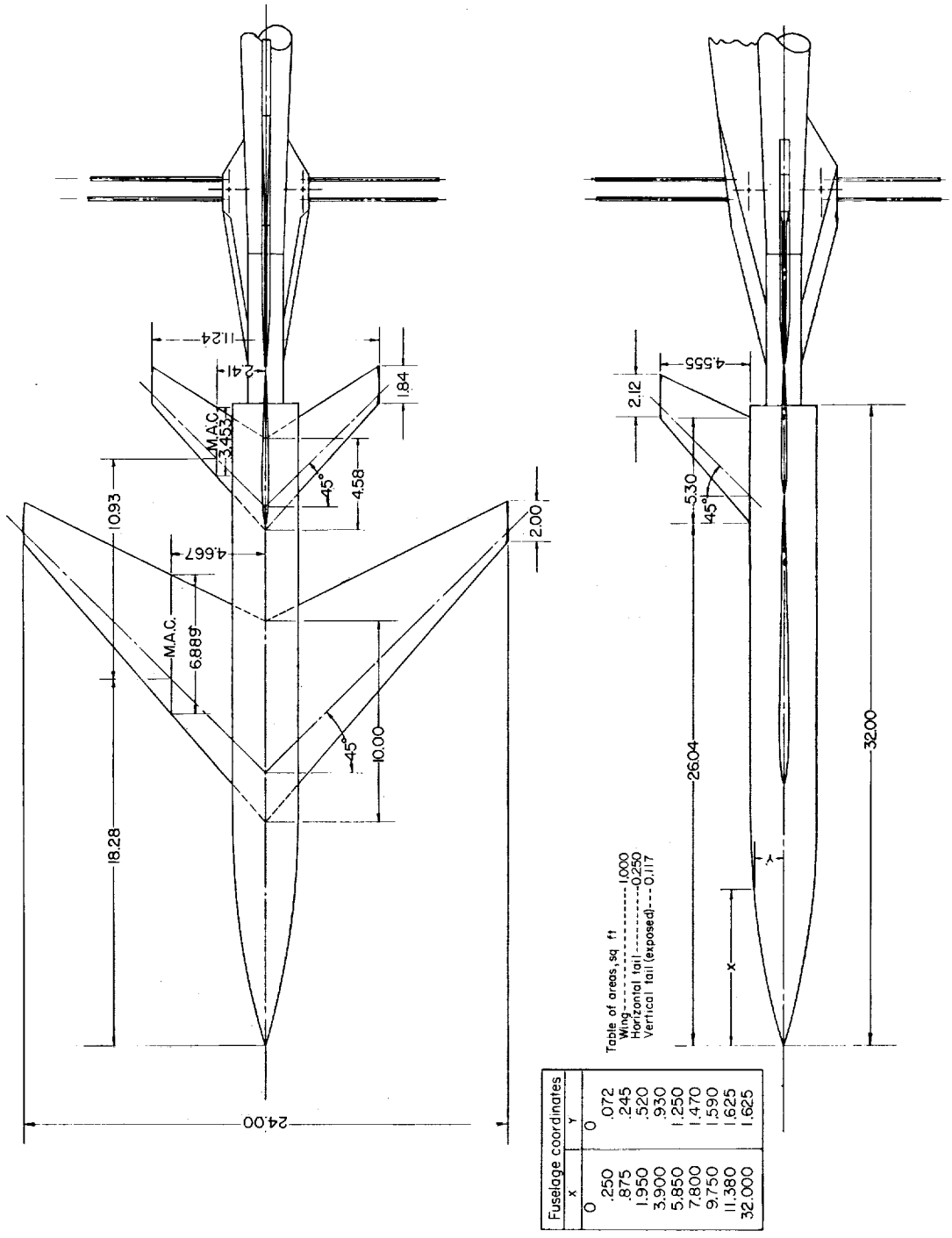

Fuselage coordinates	
x	y
0	0
.250	.072
.875	.245
1.950	.520
3.900	.930
5.850	1.250
7.800	1.470
9.750	1.590
11.380	1.625
32.000	1.625

Figure 4.- Sketch of model. All dimensions are in inches.

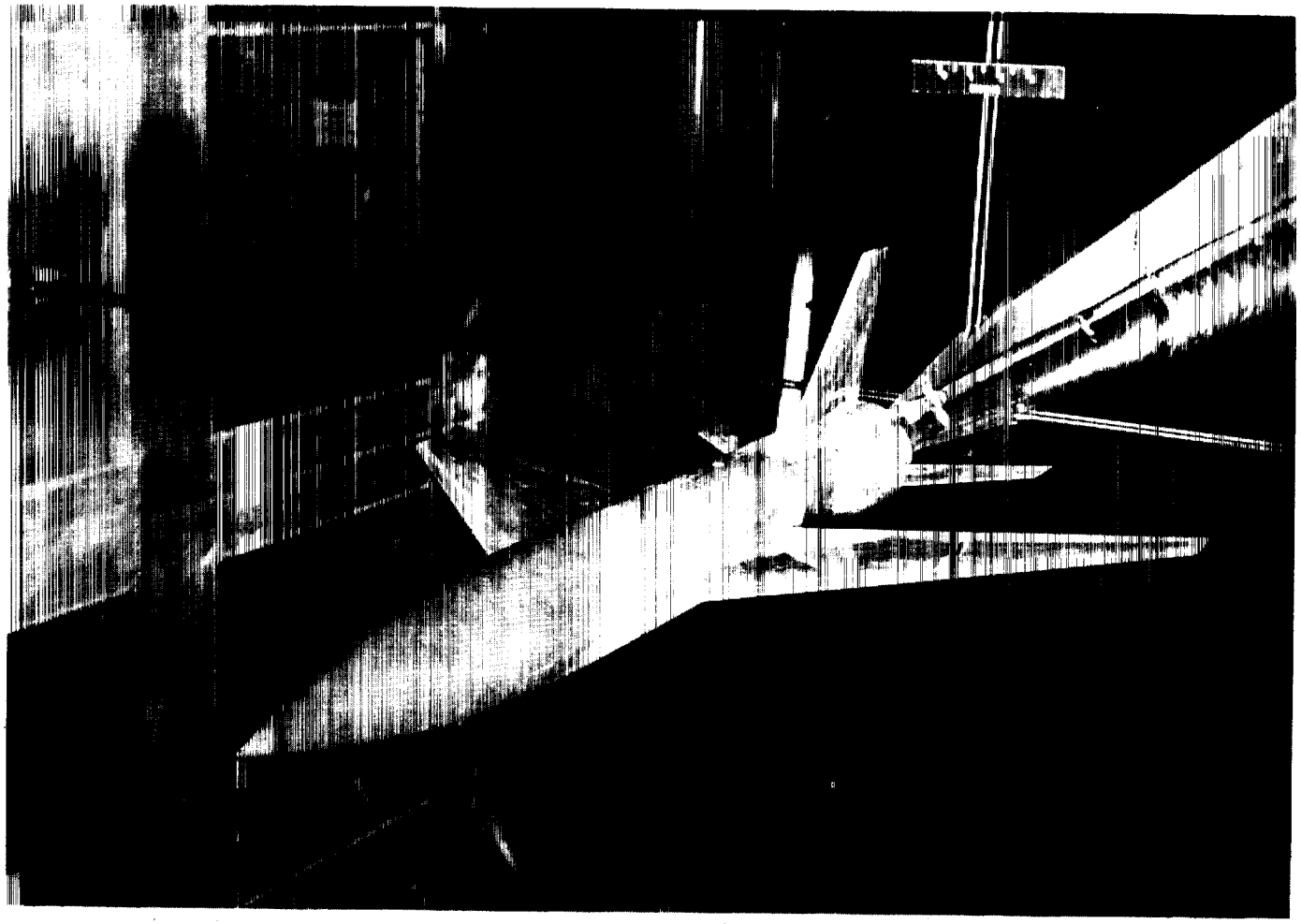

L-57-2987

Figure 5.- Model, sting support, and stiffeners mounted in wind tunnel.

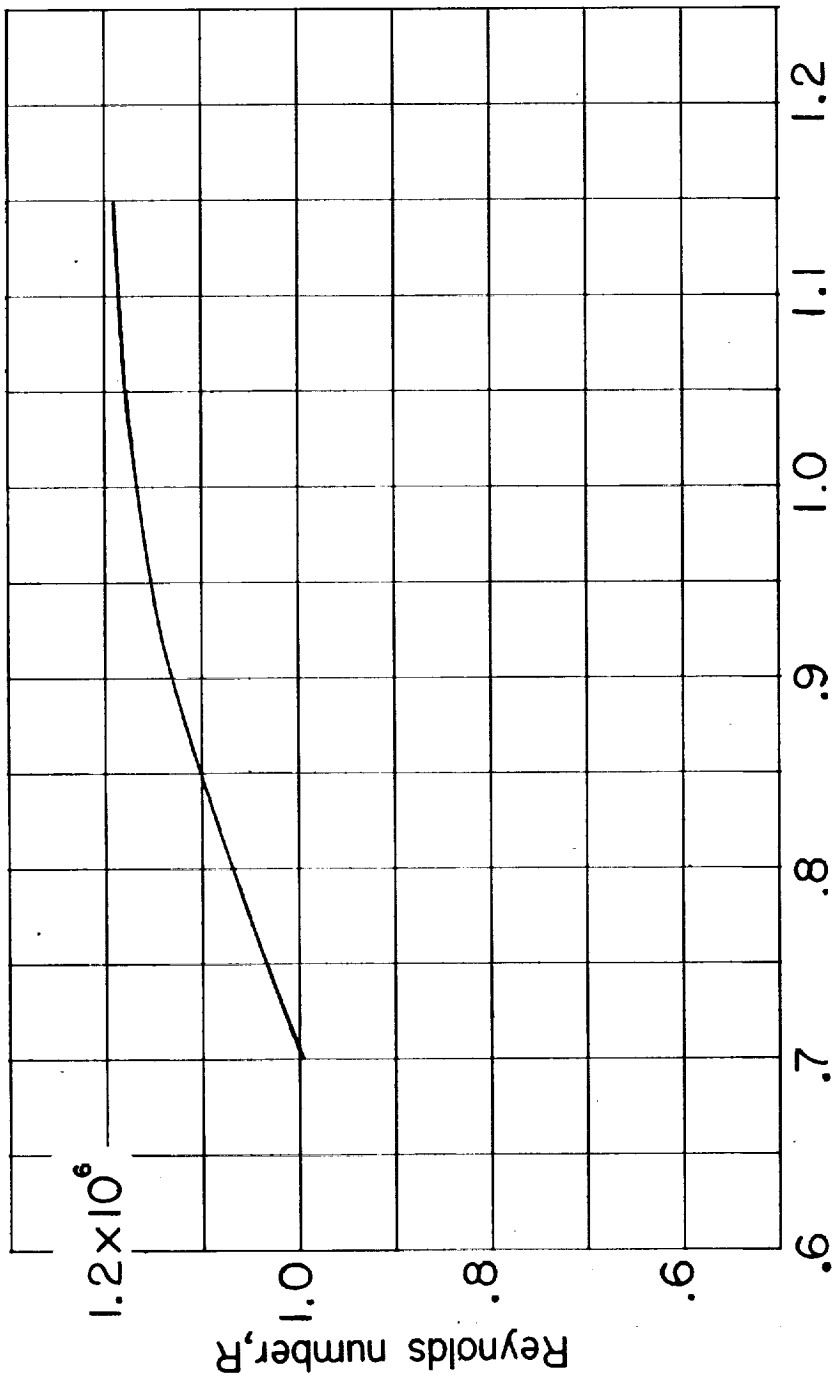

Figure 6.- Variation with Mach number of Reynolds number based on wing mean aerodynamic chord.

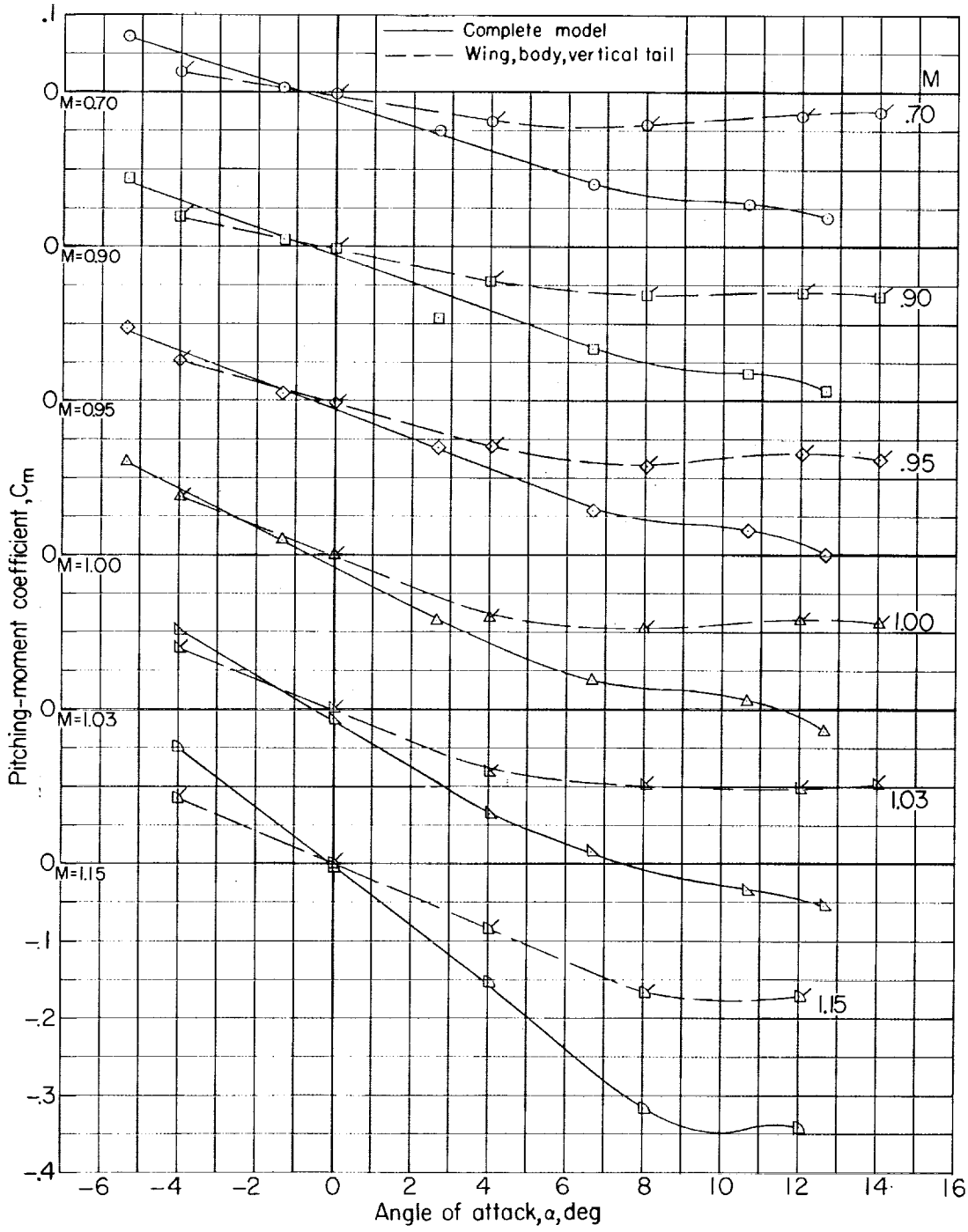

Figure 7.- Variation of static-pitching-moment coefficient with angle of attack α for complete model and for wing-body—vertical-tail configuration.

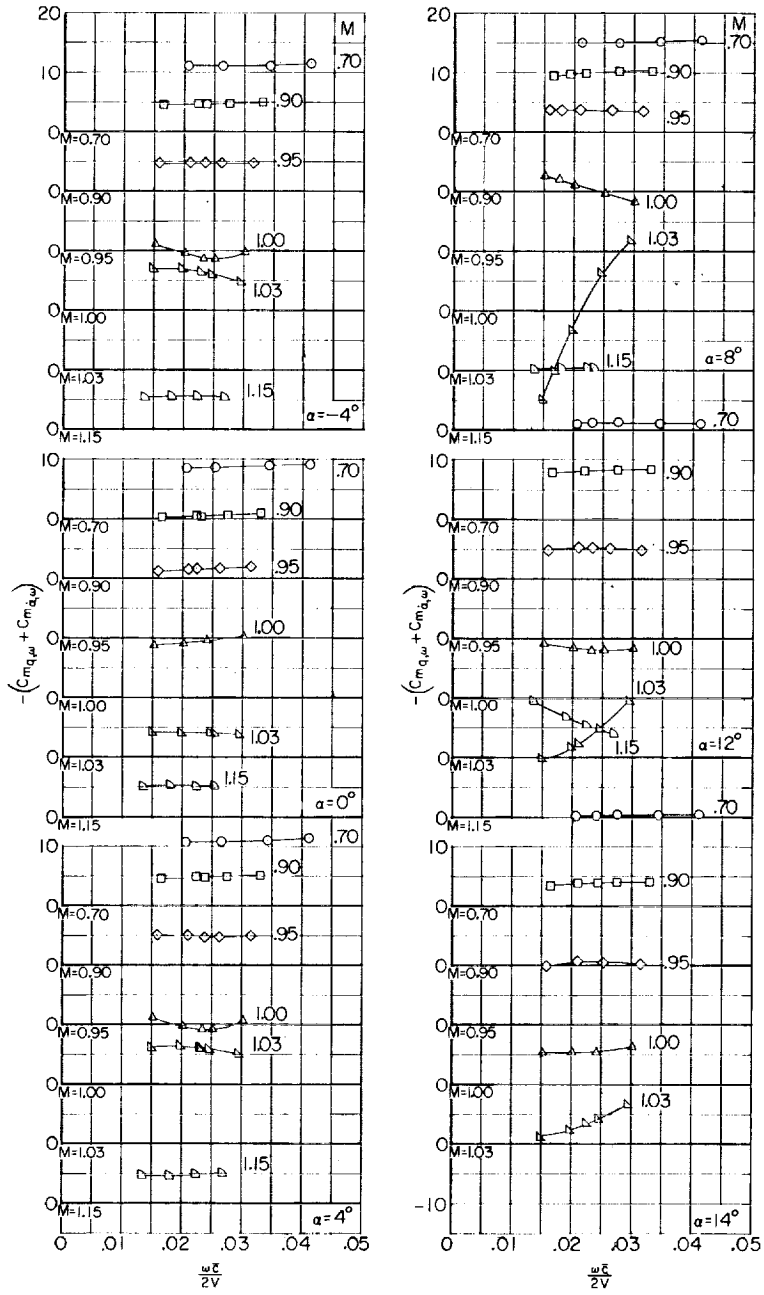

Figure 8.- Variation of damping-in-pitch derivative $C_{m_{q,\omega}} + C_{m_{\dot{\alpha},\omega}}$ with reduced-frequency parameter $\omega\bar{c}/2V$ for complete model.

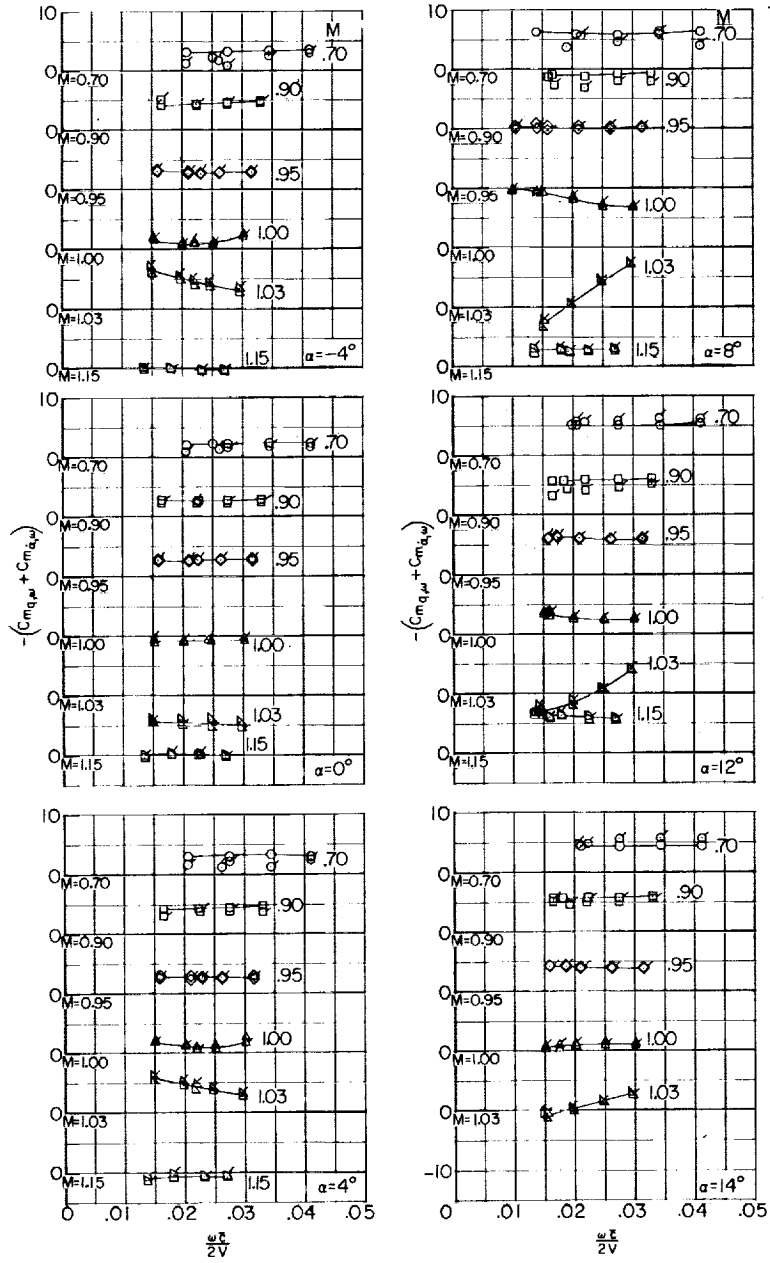

Figure 9.- Variation of damping-in-pitch derivative $C_{m_{q,\omega}} + C_{m_{\dot{\alpha},\omega}}$ with reduced-frequency parameter $\omega\bar{c}/2V$ for wing-body—vertical-tail configuration. Flagged symbols represent repeat data.

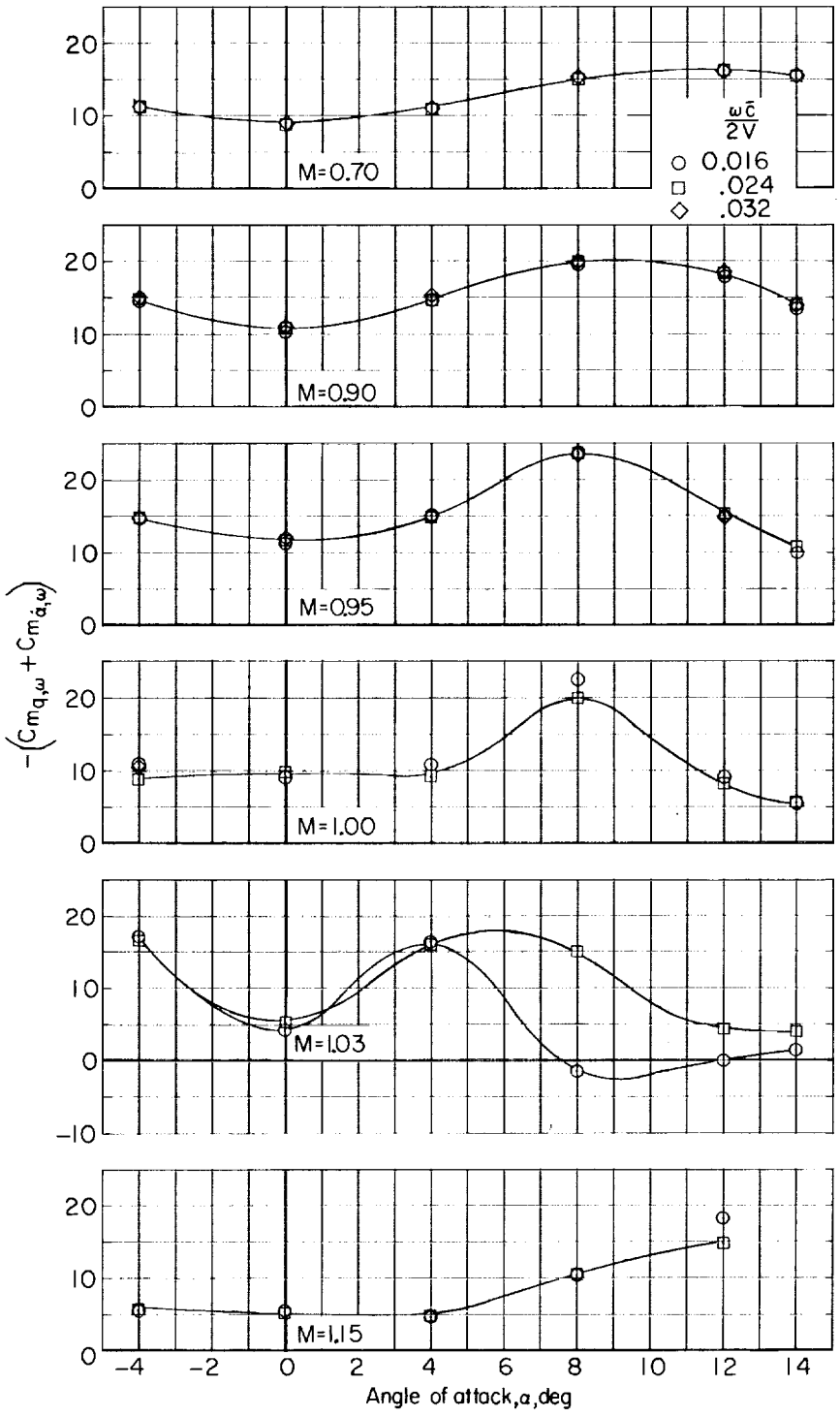

Figure 10.- Variation of $C_{m_{q,\omega}} + C_{m_{\dot{\alpha},\omega}}$ with angle of attack α for various Mach numbers for complete model.

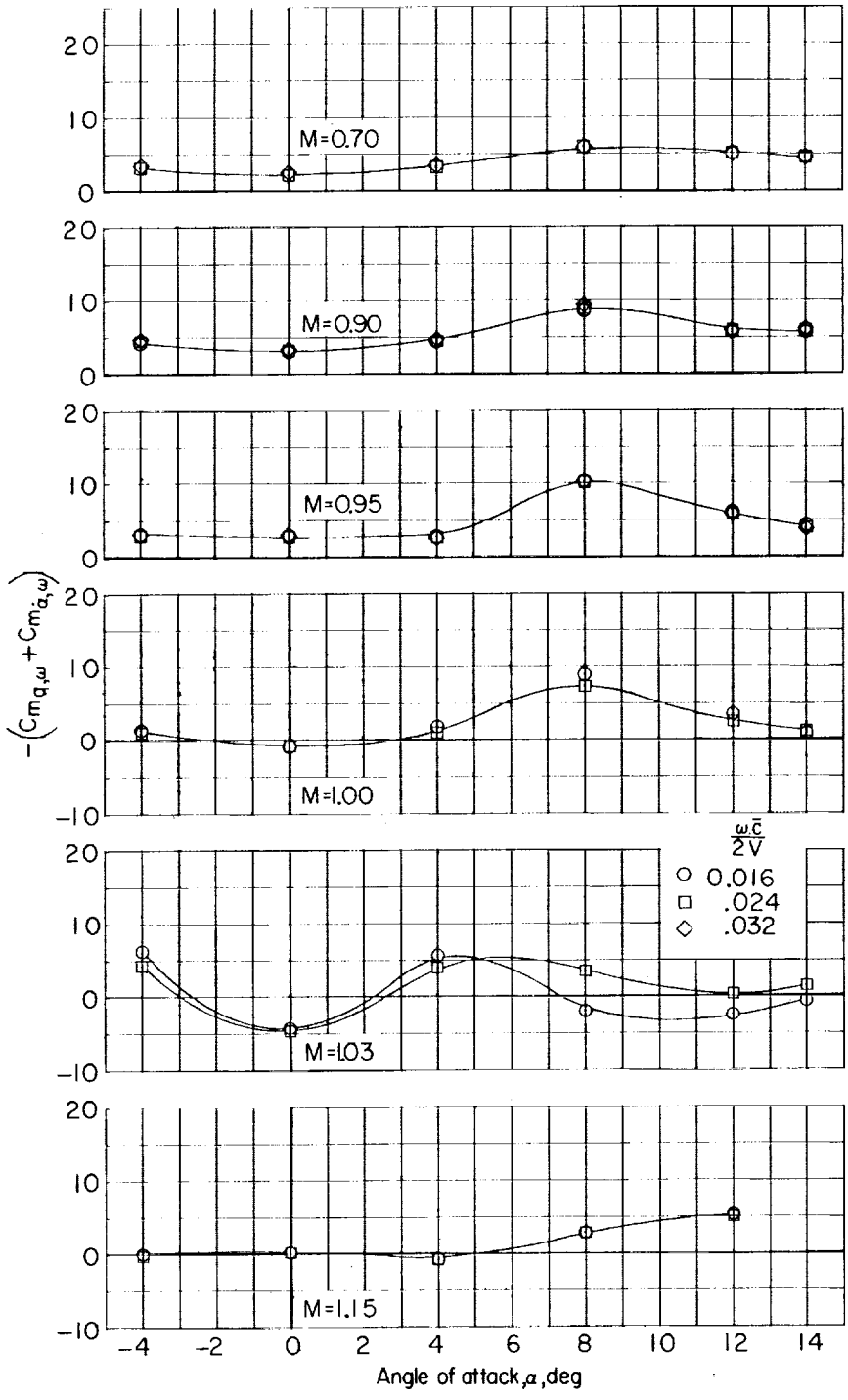

Figure 11.- Variation of $C_{m_{q,\omega}} + C_{m_{\dot{\alpha},\omega}}$ with angle of attack α for various Mach numbers for wing-body—vertical-tail configuration.

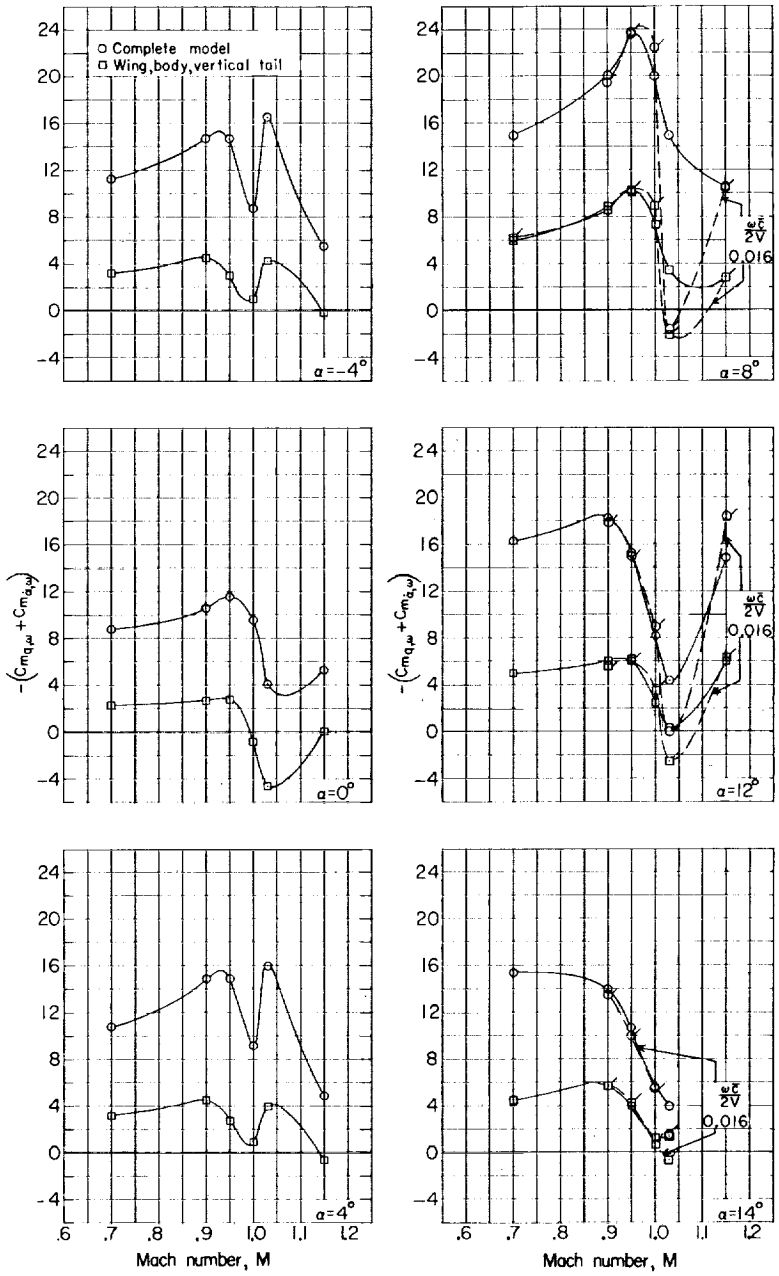

Figure 12.- Variation of $C_{m_{q,\omega}} + C_{m_{\dot{\alpha},\omega}}$ with Mach number M for complete model and wing-body—vertical-tail configuration. $\omega\bar{c}/2V = 0.024$, except as noted.

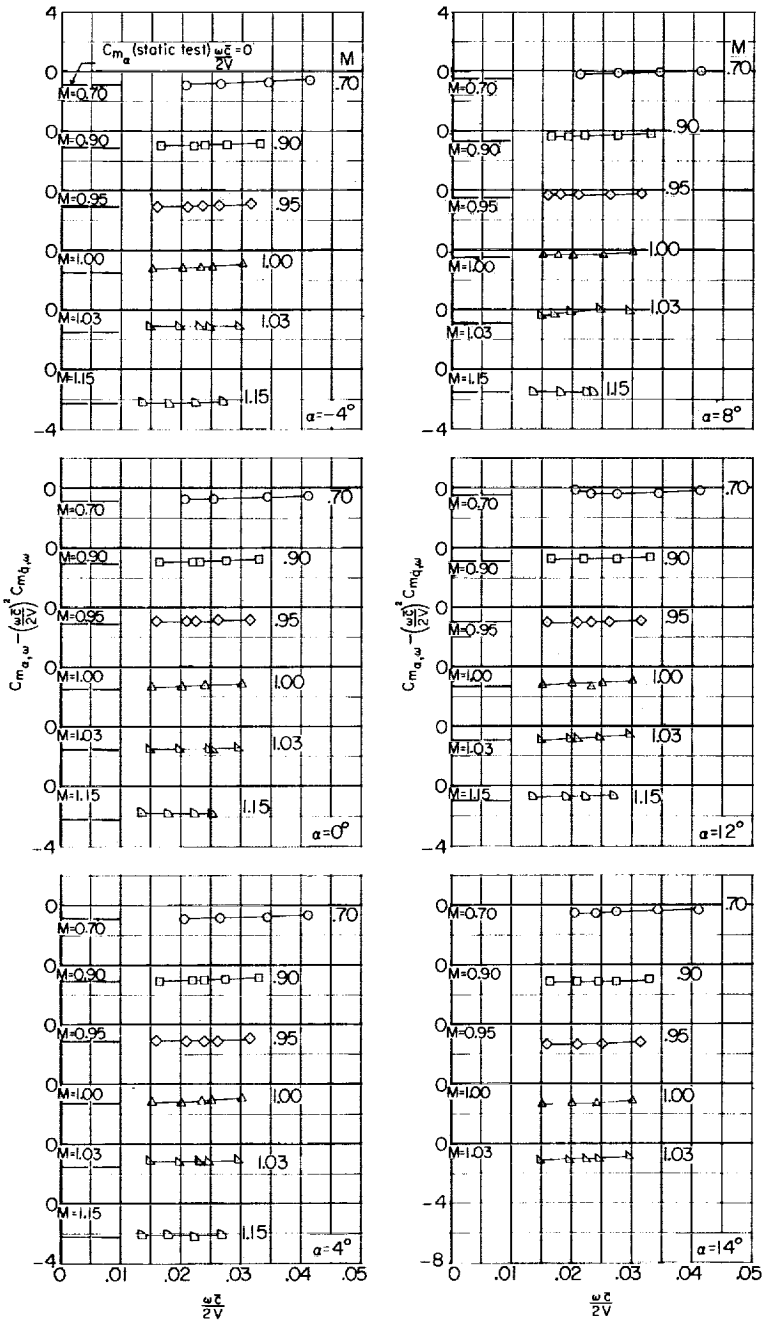

Figure 13.- Variation of oscillatory longitudinal stability derivative $C_{m_{\alpha,\omega}} - \left(\frac{\omega\bar{c}}{2V}\right)^2 C_{m_{q,\omega}}$ with reduced-frequency parameter $\omega\bar{c}/2V$ for complete model.

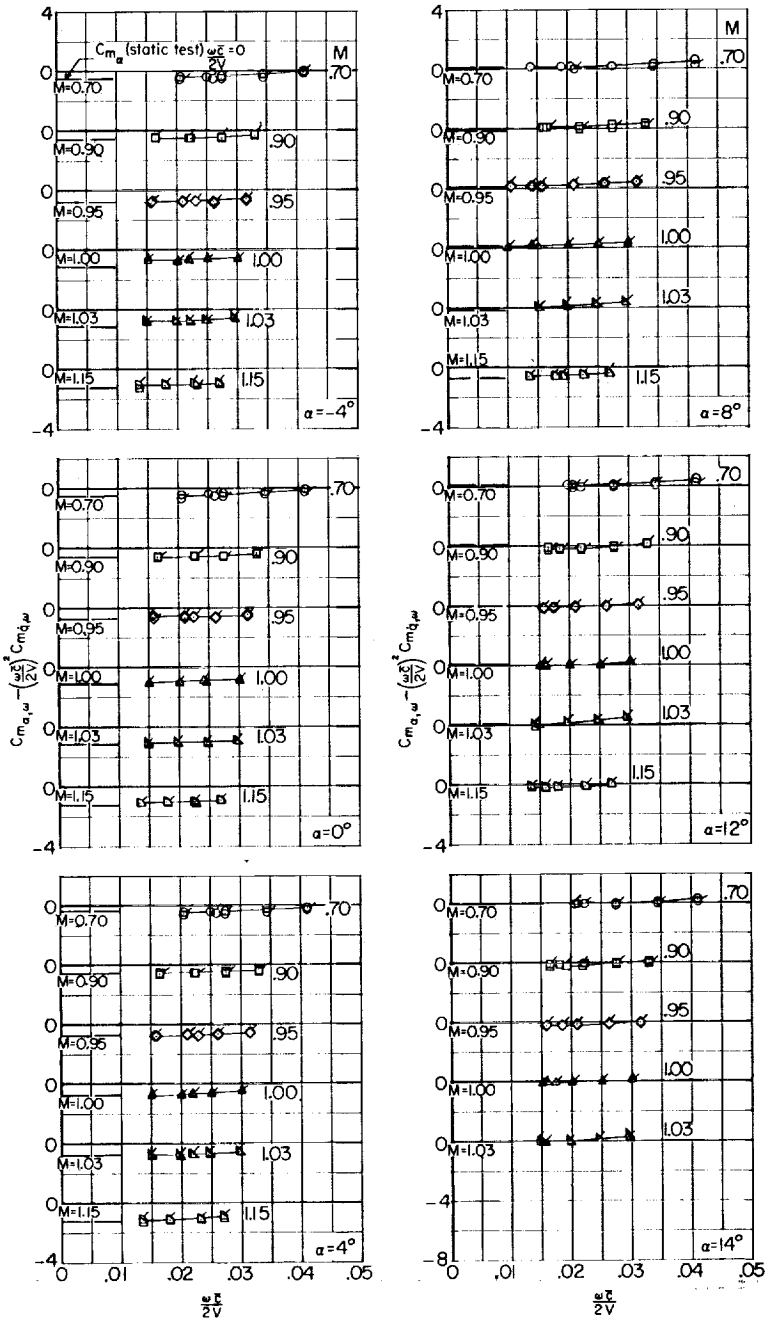

Figure 14.- Variation of oscillatory longitudinal stability derivative $C_{m_{\alpha,\omega}} - \left(\frac{\omega\bar{c}}{2V}\right)^2 C_{m_{\dot{q},\omega}}$ with reduced-frequency parameter $\omega\bar{c}/2V$ for wing-body—vertical-tail configuration. Flagged symbols represent repeat data.

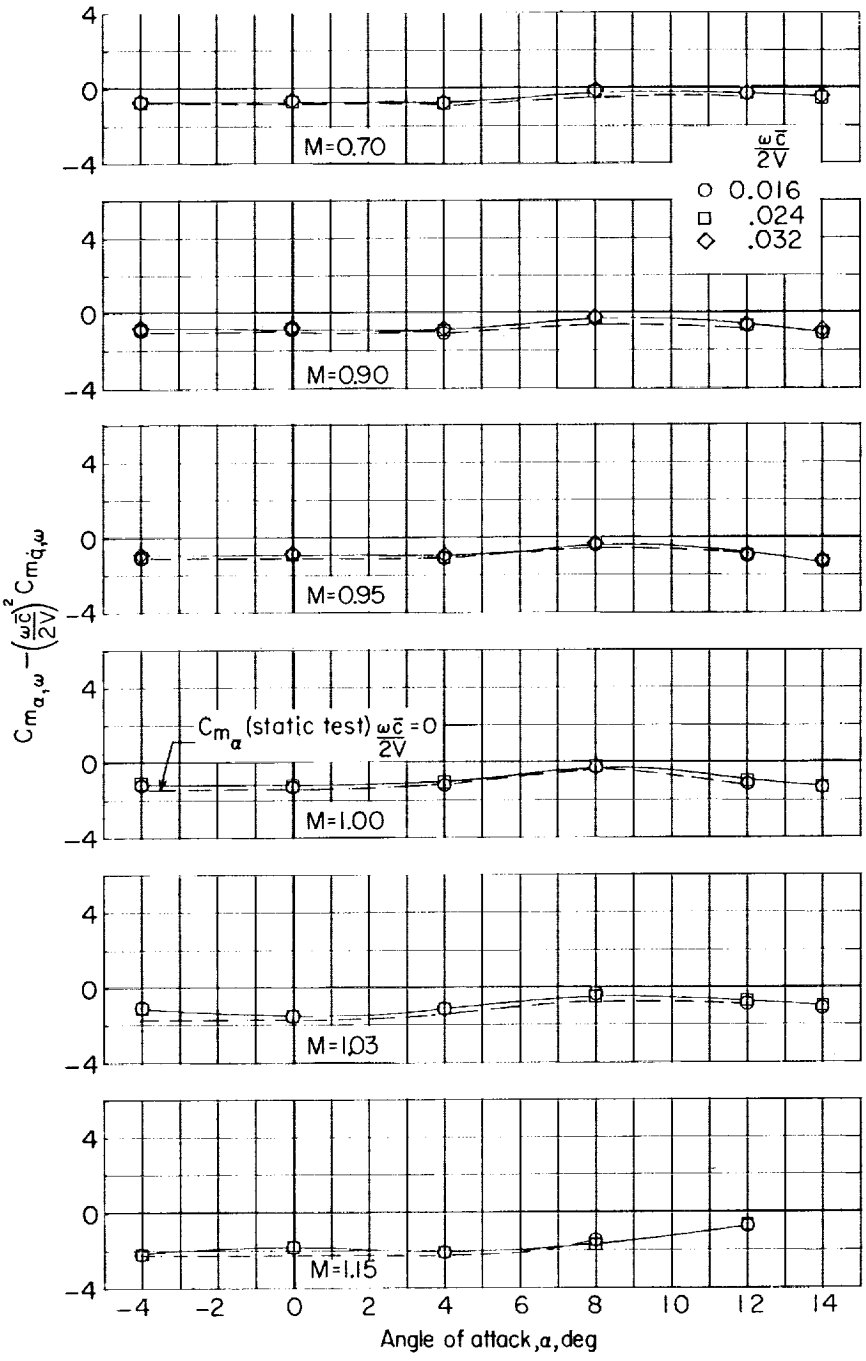

Figure 15.- Variation of $C_{m_{\alpha,\omega}} - \left(\frac{\omega\bar{c}}{2V}\right)^2 C_{m_{\dot{q},\omega}}$ with angle of attack α for various Mach numbers for complete model.

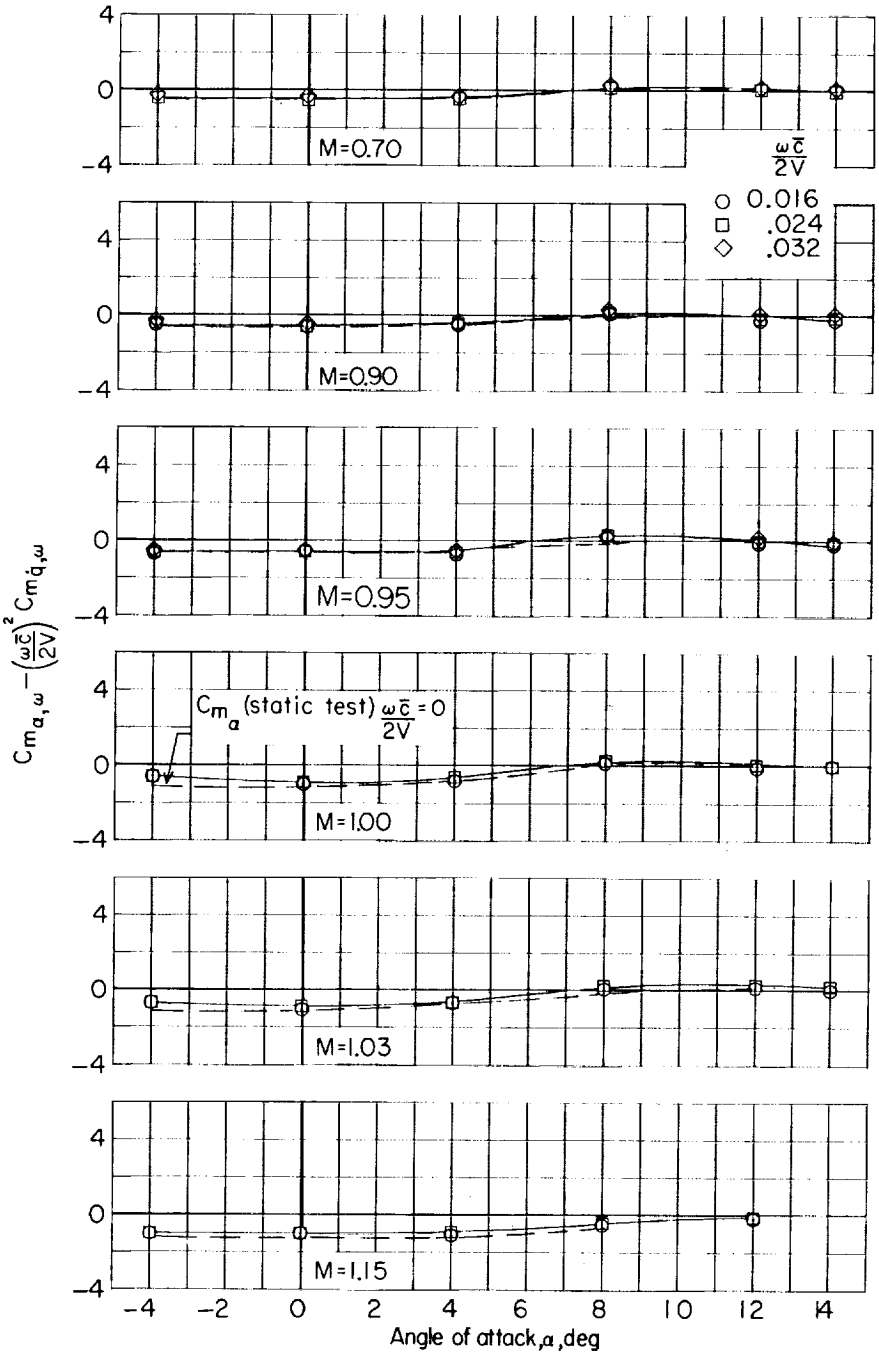

Figure 16.- Variation of $C_{m_{\alpha,\omega}} - \left(\frac{\omega\bar{c}}{2V}\right)^2 C_{m_{\dot{q},\omega}}$ with angle of attack α for various Mach numbers for wing-body—vertical-tail configuration.

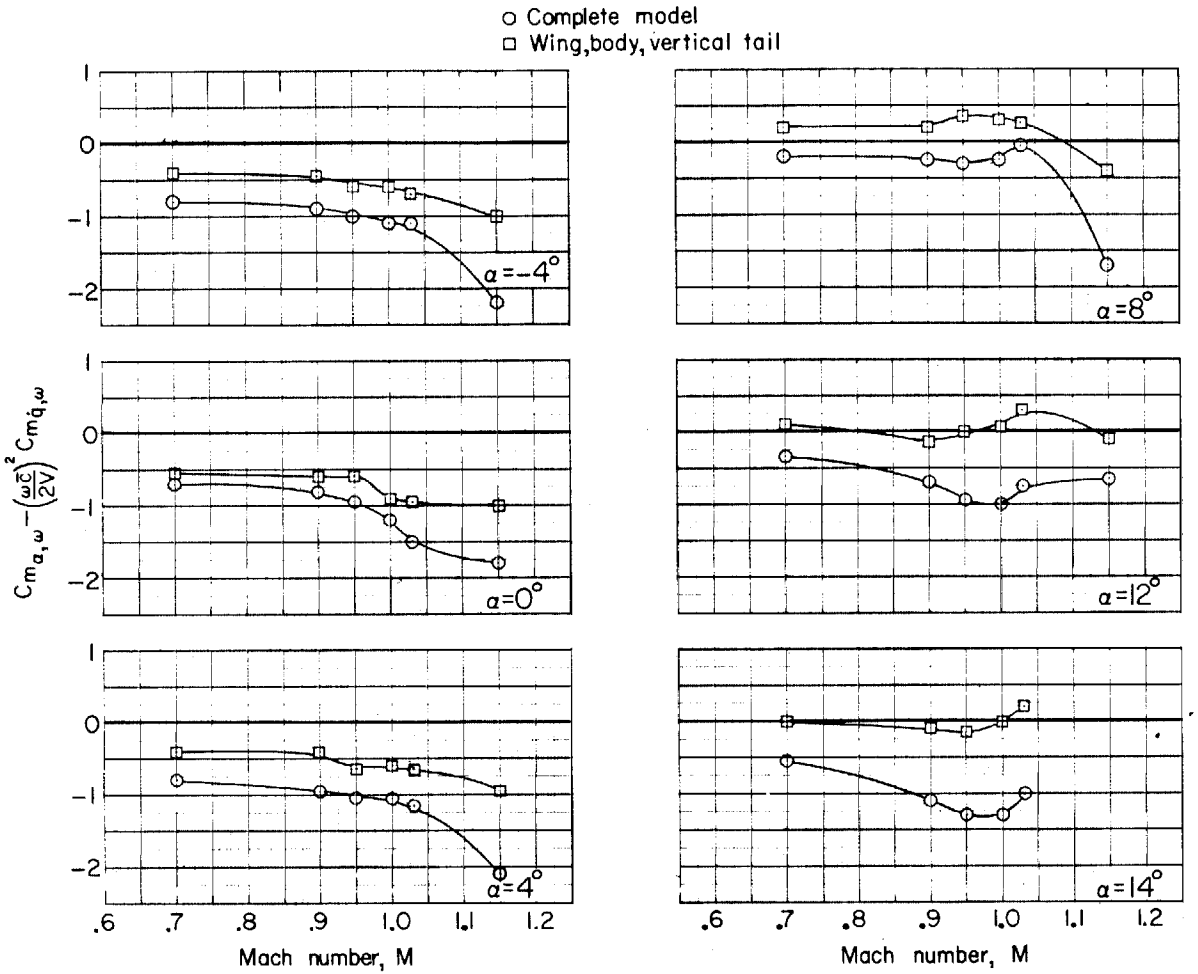

Figure 17.- Variation of $C_{m_{\alpha,\omega}} - \left(\frac{\omega\bar{c}}{2V}\right)^2 C_{m_{\dot{q},\omega}}$ with Mach number M for complete model and wing-body—vertical-tail configuration. $\omega\bar{c}/2V = 0.024$.

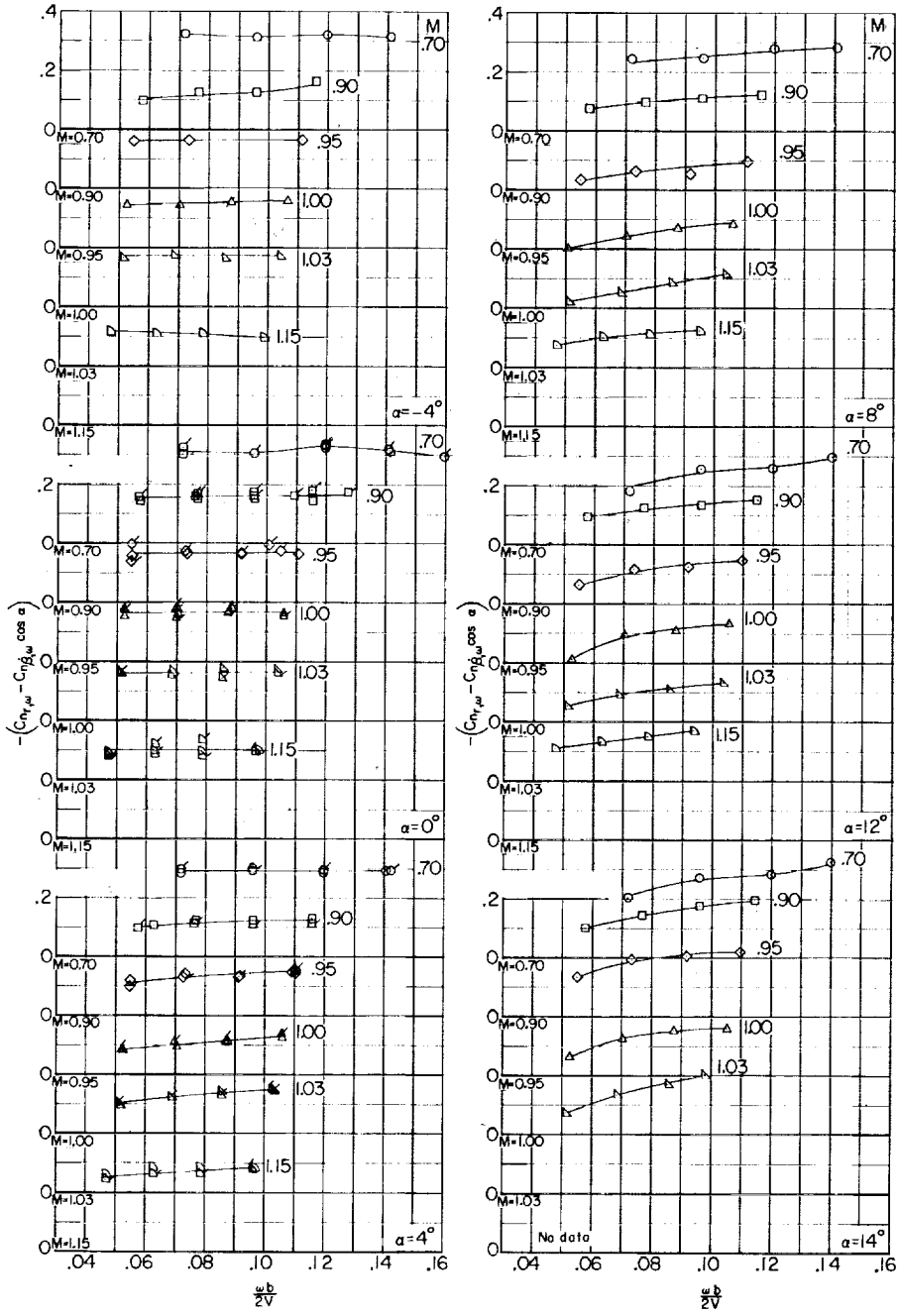

Figure 18.- Variation of damping-in-yaw derivative $C_{n_{r,\omega}} - C_{n_{\dot{\beta},\omega}} \cos \alpha$ with reduced-frequency parameter $\omega b/2V$ for complete model. Flagged symbols represent repeat data.

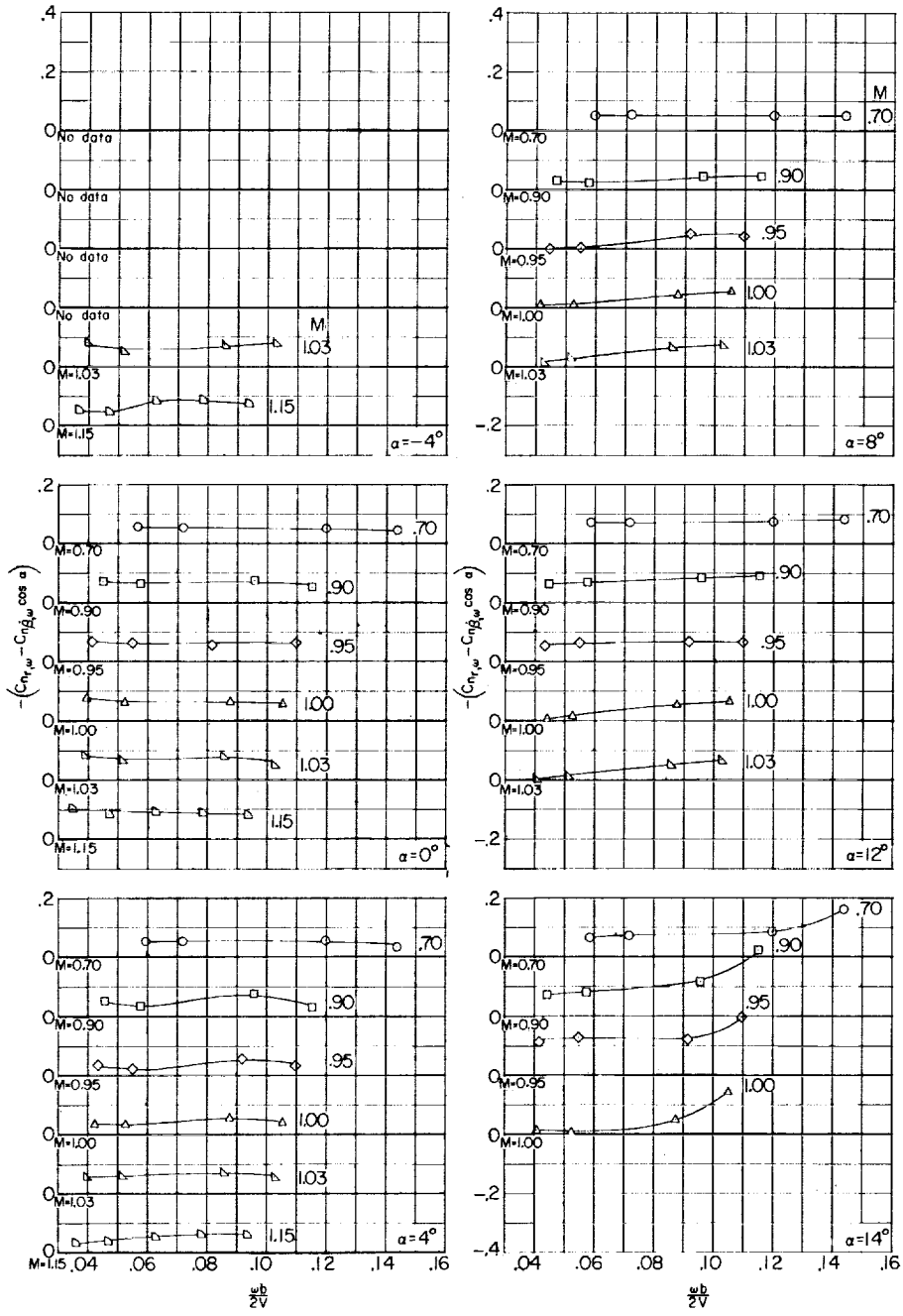

Figure 19.- Variation of damping-in-yaw derivative $C_{n_{r,\omega}} - C_{n_{\dot{\beta},\omega}} \cos\alpha$ with reduced-frequency parameter $\omega b/2V$ for wing-body—horizontal-tail configuration.

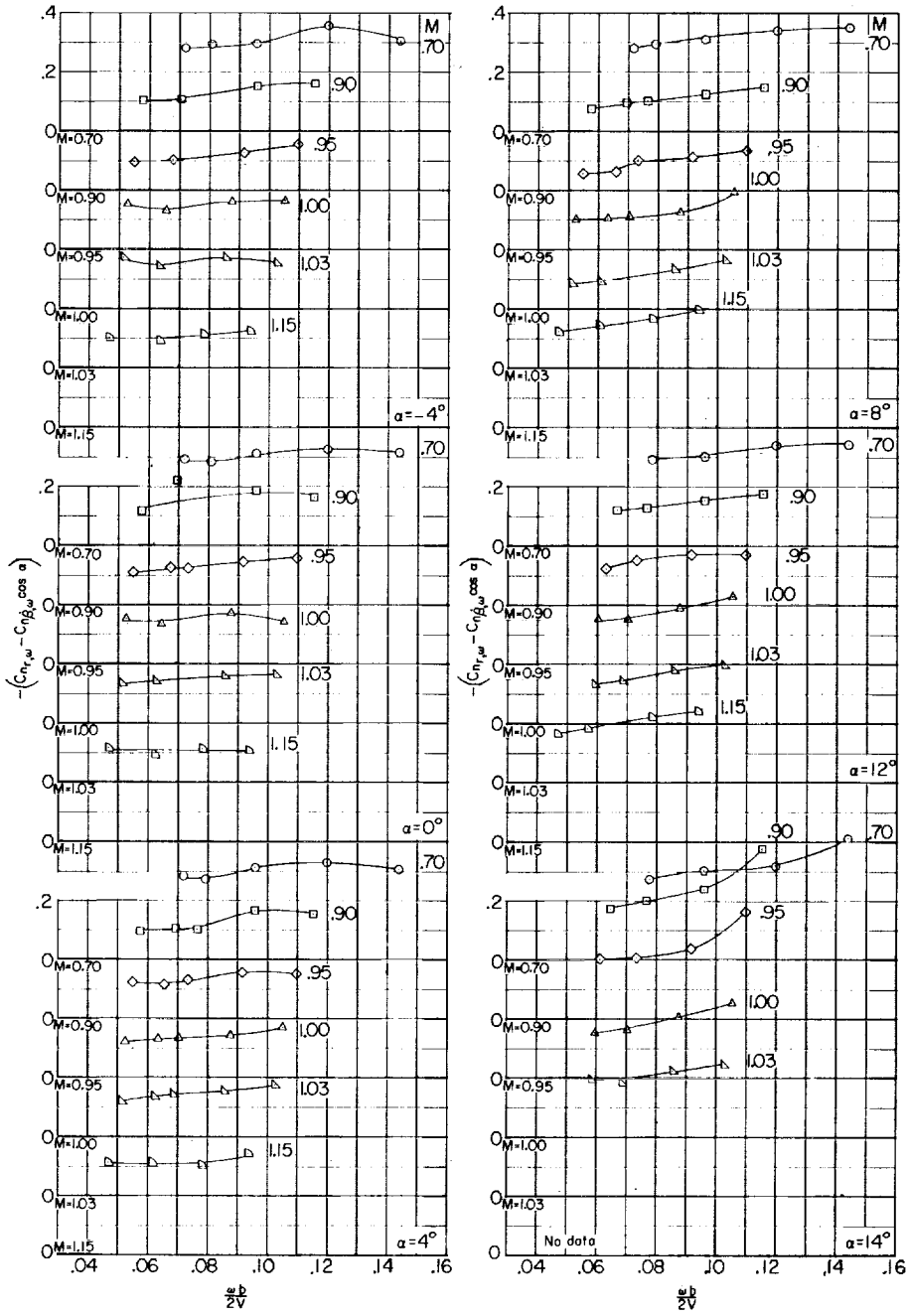

Figure 20.- Variation of damping-in-yaw derivative $C_{n_{r,\omega}} - C_{n_{\dot{\beta},\omega}} \cos\alpha$ with reduced-frequency parameter $\omega b/2V$ for wing-body—vertical-tail configuration.

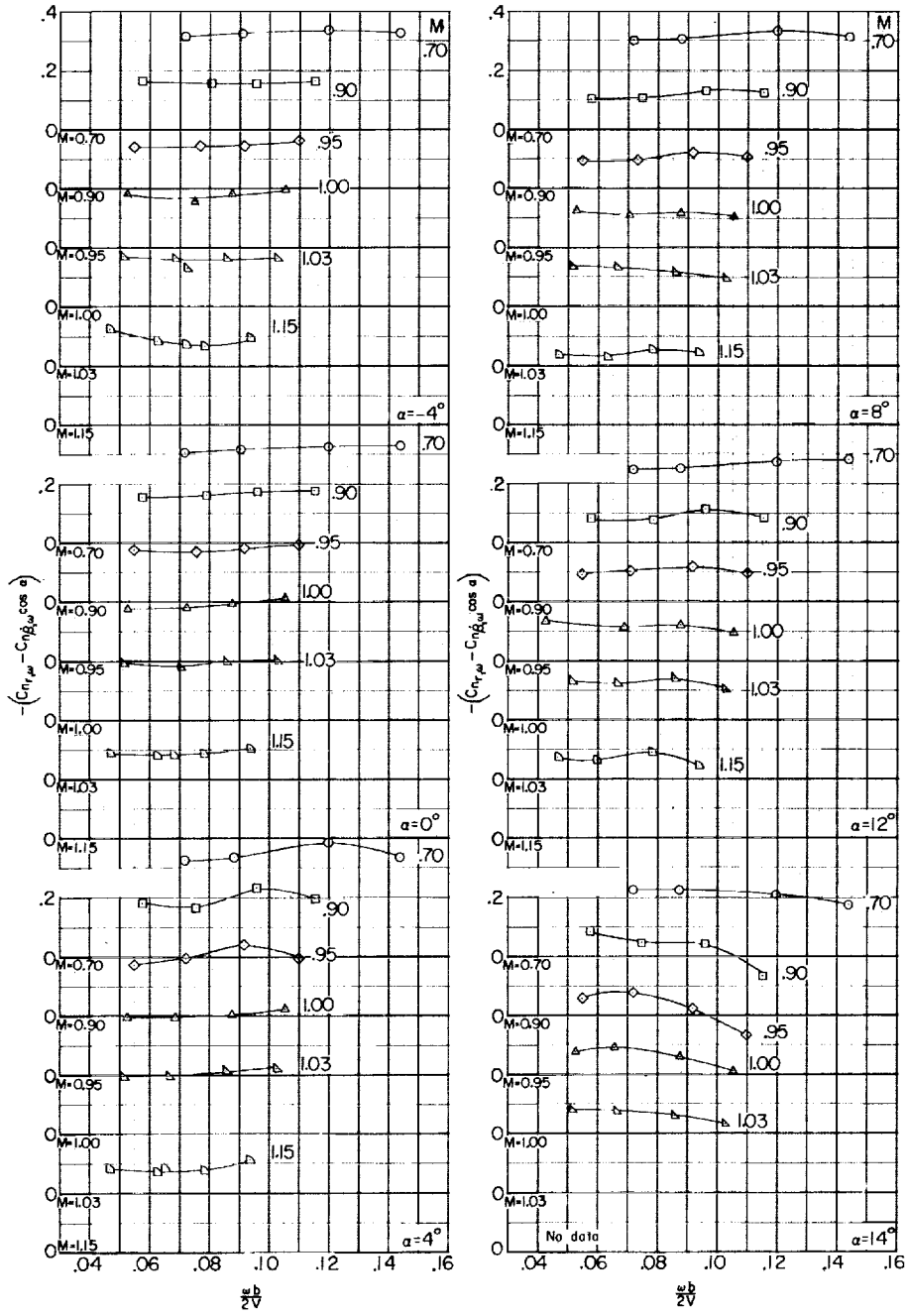

Figure 21.- Variation of damping-in-yaw derivative $C_{n_{r,\omega}} - C_{n_{\dot{\beta},\omega}} \cos\alpha$ with reduced-frequency parameter $\omega b/2V$ for configuration having a body, horizontal tail, and vertical tail.

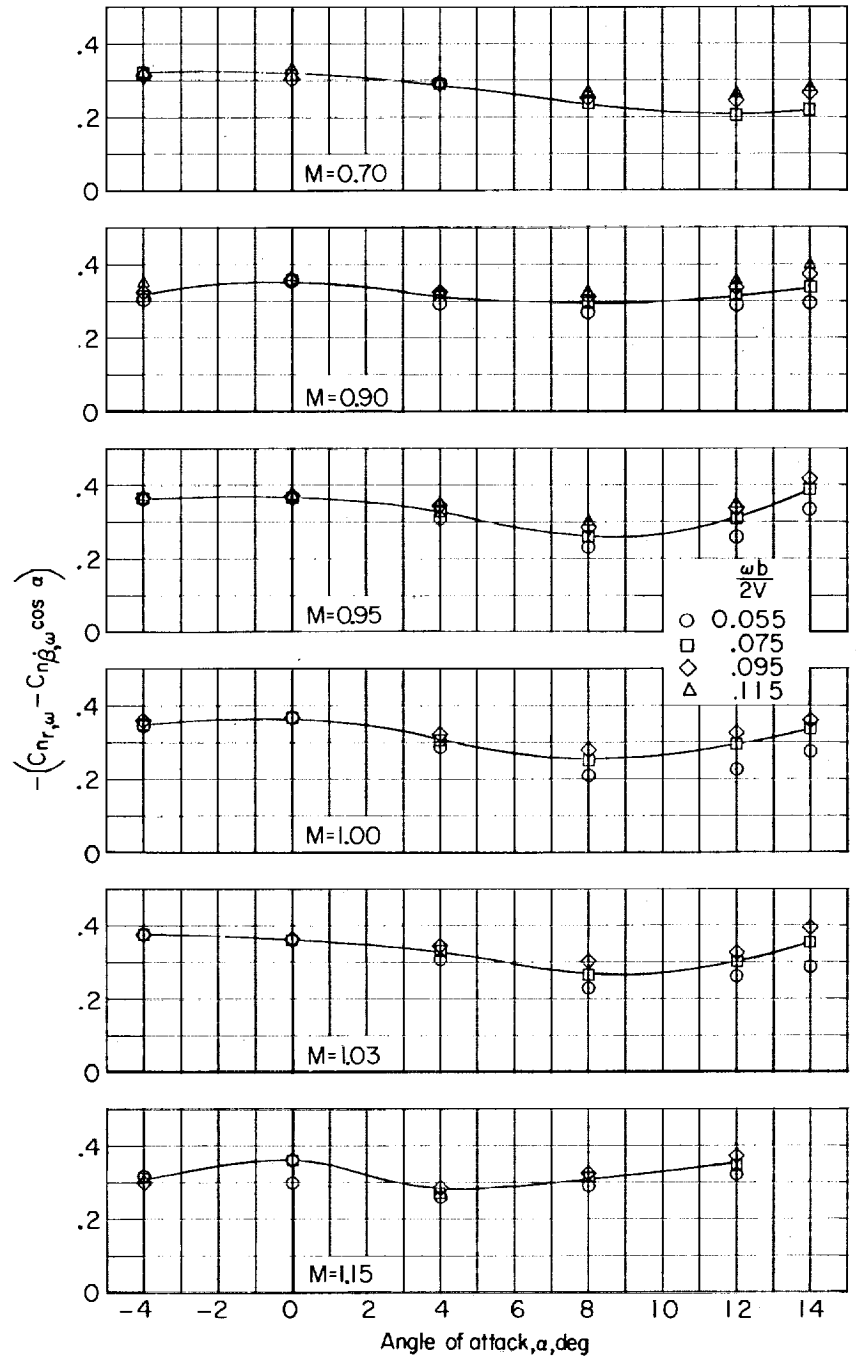

Figure 22.- Variation of $C_{n_{r,\omega}} - C_{n_{\dot{\beta},\omega}} \cos \alpha$ with angle of attack α for various Mach numbers for complete model.

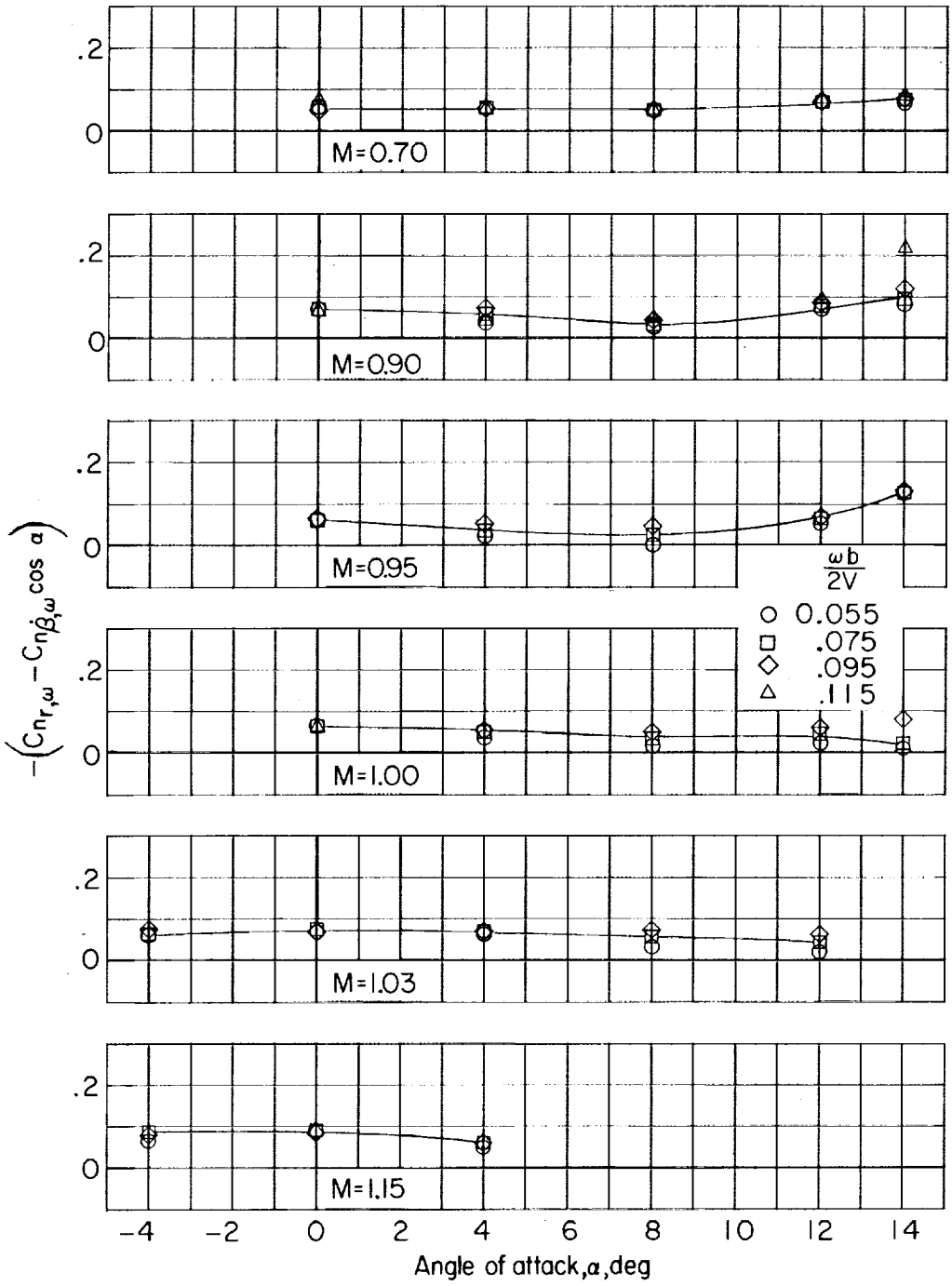

Figure 23.- Variation of $C_{n_{r,\omega}} - C_{n_{\dot{\beta},\omega}} \cos \alpha$ with angle of attack α for various Mach numbers for wing-body—horizontal-tail configuration.

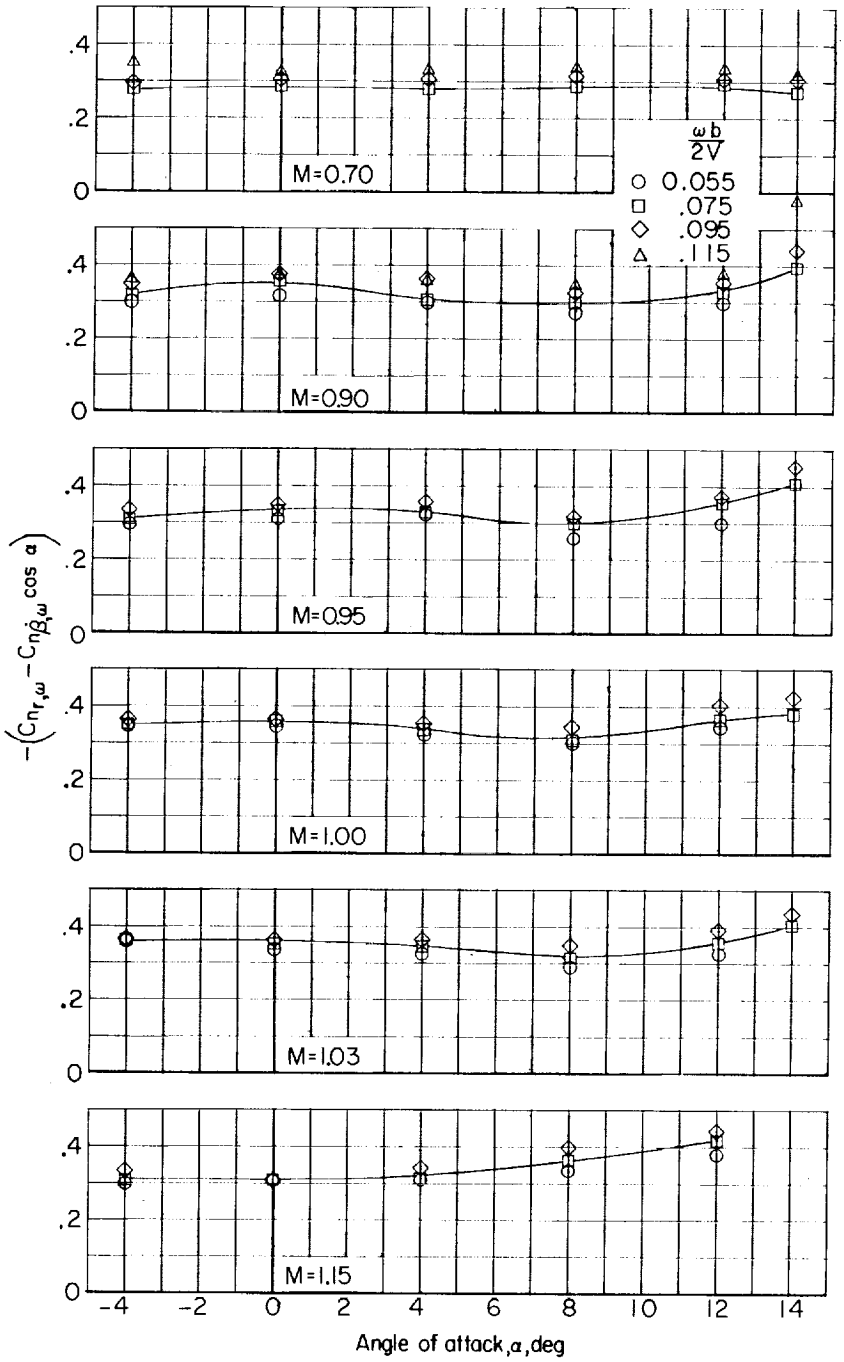

Figure 24.- Variation of $C_{n_{r,\omega}} - C_{n_{\dot{\beta},\omega}} \cos \alpha$ with angle of attack α for various Mach numbers for wing-body—vertical-tail configuration.

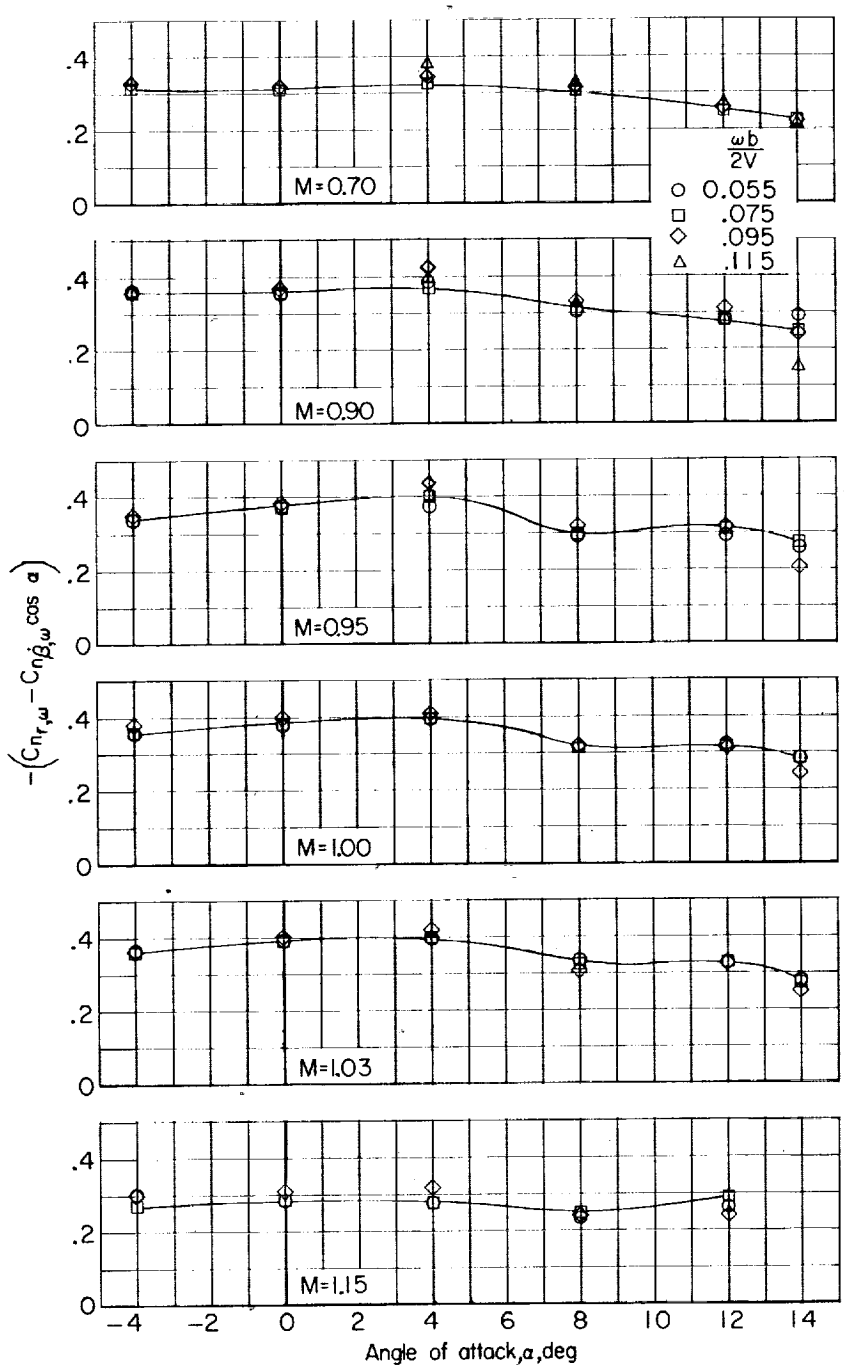

Figure 25.- Variation of $C_{n_{r,\omega}} - C_{n_{\dot{\beta},\omega}} \cos \alpha$ with angle of attack α for various Mach numbers for configuration having a body, horizontal tail, and vertical tail.

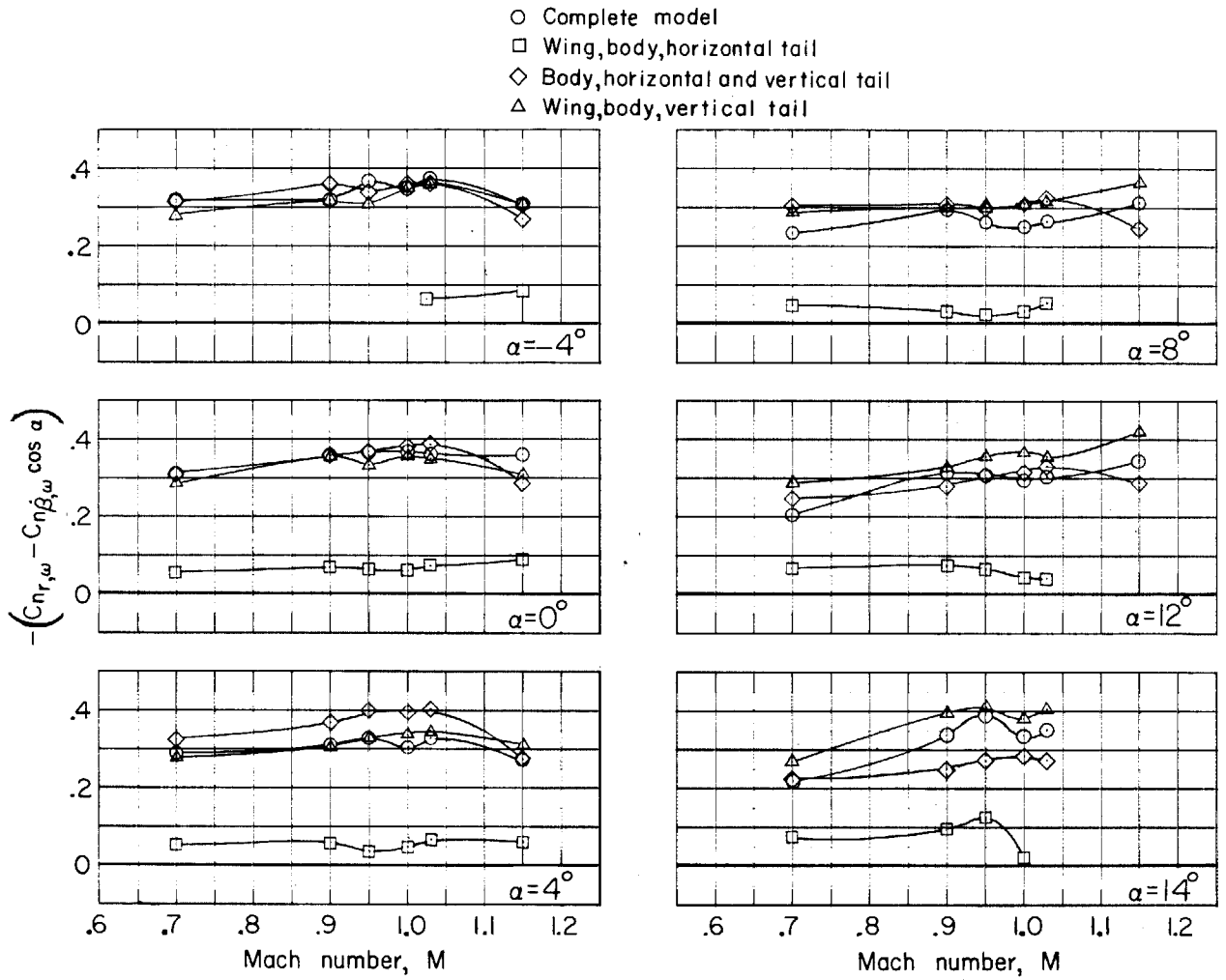

Figure 26.- Variation of $C_{n_{r,\omega}} - C_{n_{\dot{\beta},\omega}} \cos \alpha$ with Mach number for various model configurations. $\omega b/2V = 0.075$.

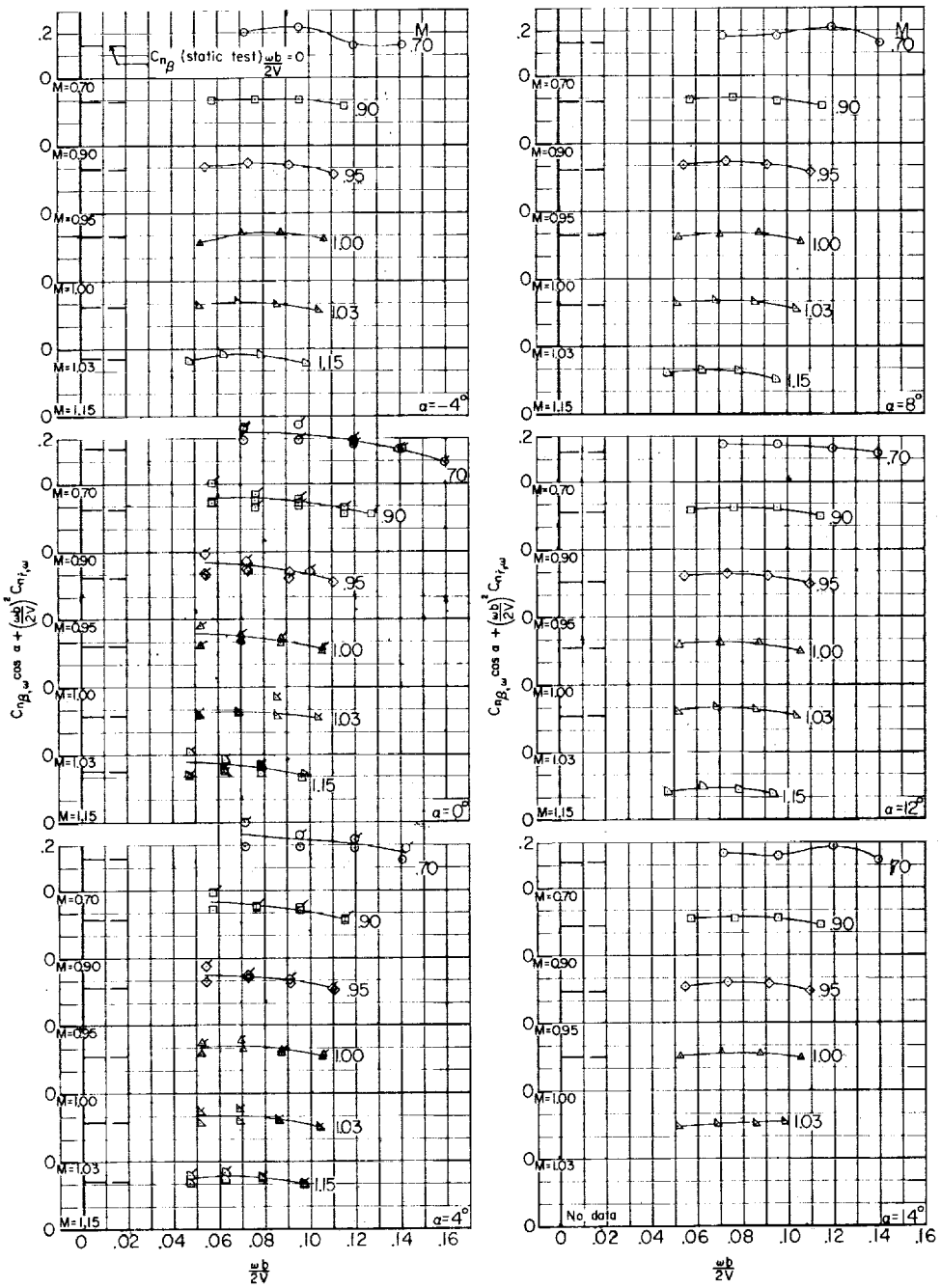

Figure 27.- Variation of oscillatory directional stability derivative $C_{n_{\beta,\omega}} \cos \alpha + \left(\frac{\omega b}{2V}\right)^2 C_{n_{\dot{r},\omega}}$ with reduced-frequency parameter $\omega b/2V$ for complete model. Flagged symbols denote repeat data.

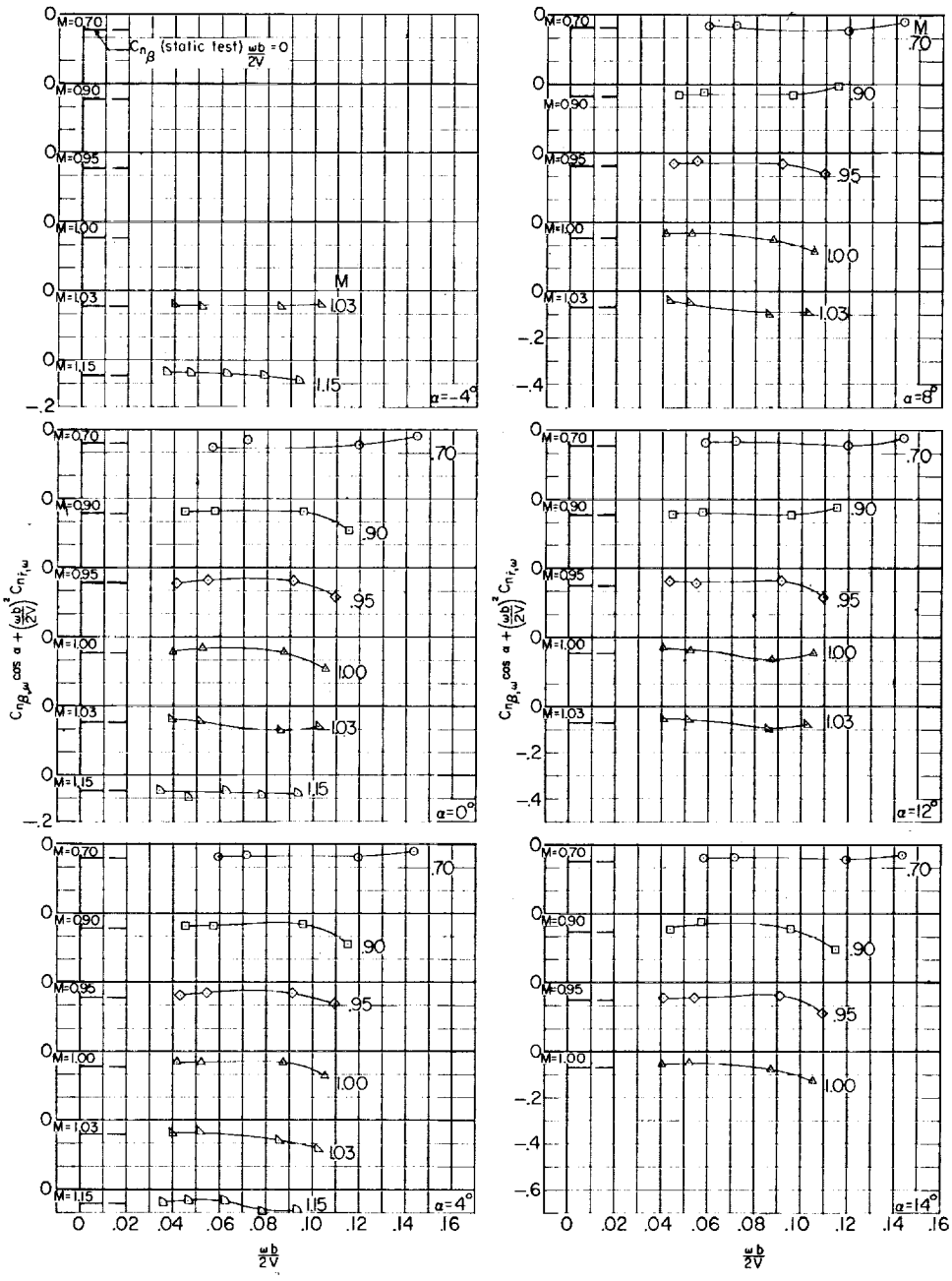

Figure 28.- Variation of oscillatory directional stability derivative $C_{n_{\beta,\omega}} \cos \alpha + \left(\frac{\omega b}{2V}\right)^2 C_{n_{\dot{r},\omega}}$ with reduced-frequency parameter $\omega b/2V$ for wing-body—horizontal-tail configuration.

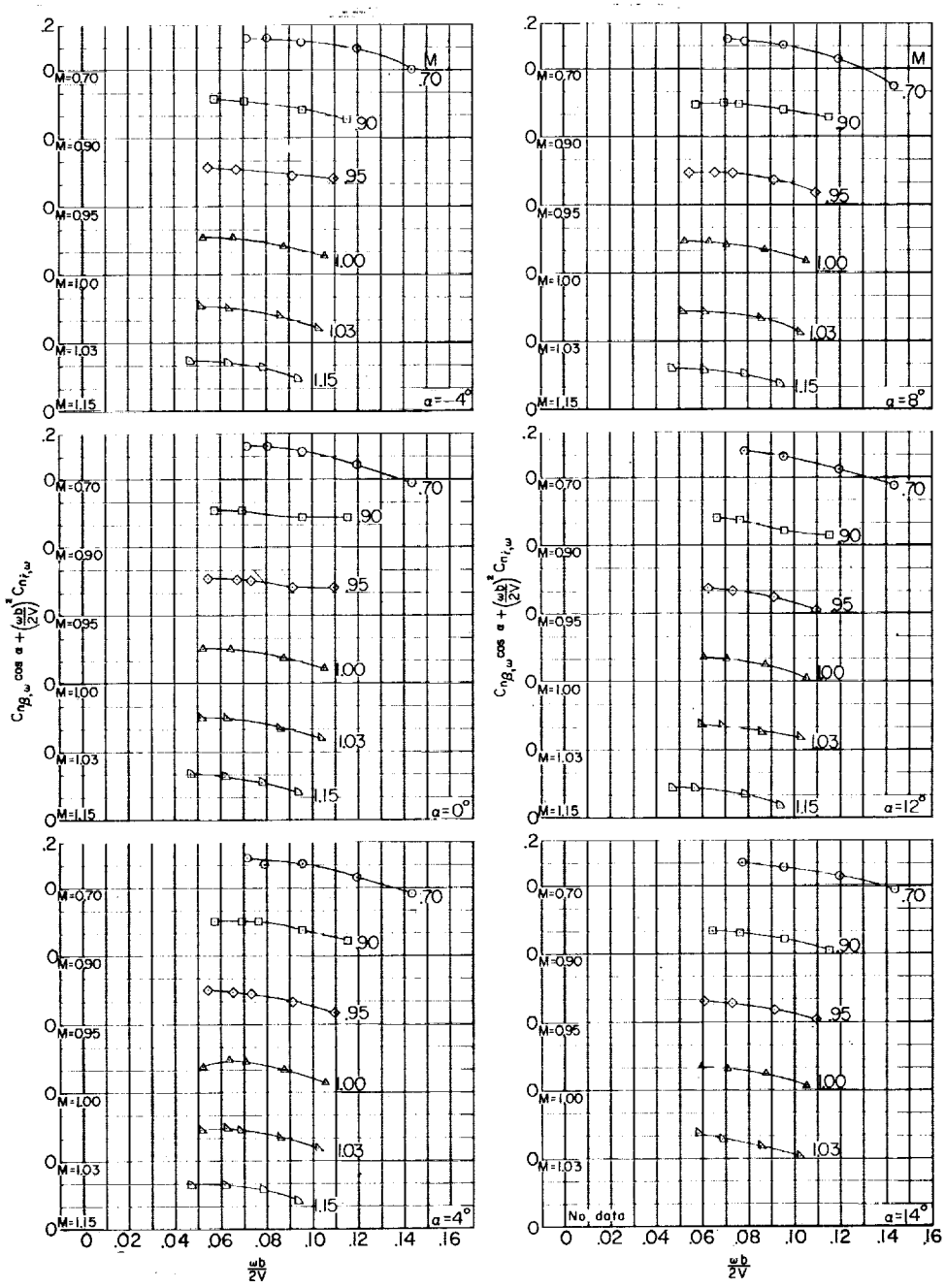

Figure 29.- Variation of oscillatory directional stability derivative $C_{n_{\beta,\omega}} \cos\alpha + \left(\frac{\omega b}{2V}\right)^2 C_{n_{\dot{r},\omega}}$ with reduced-frequency parameter $\omega b/2V$ for wing-body—vertical-tail configuration.

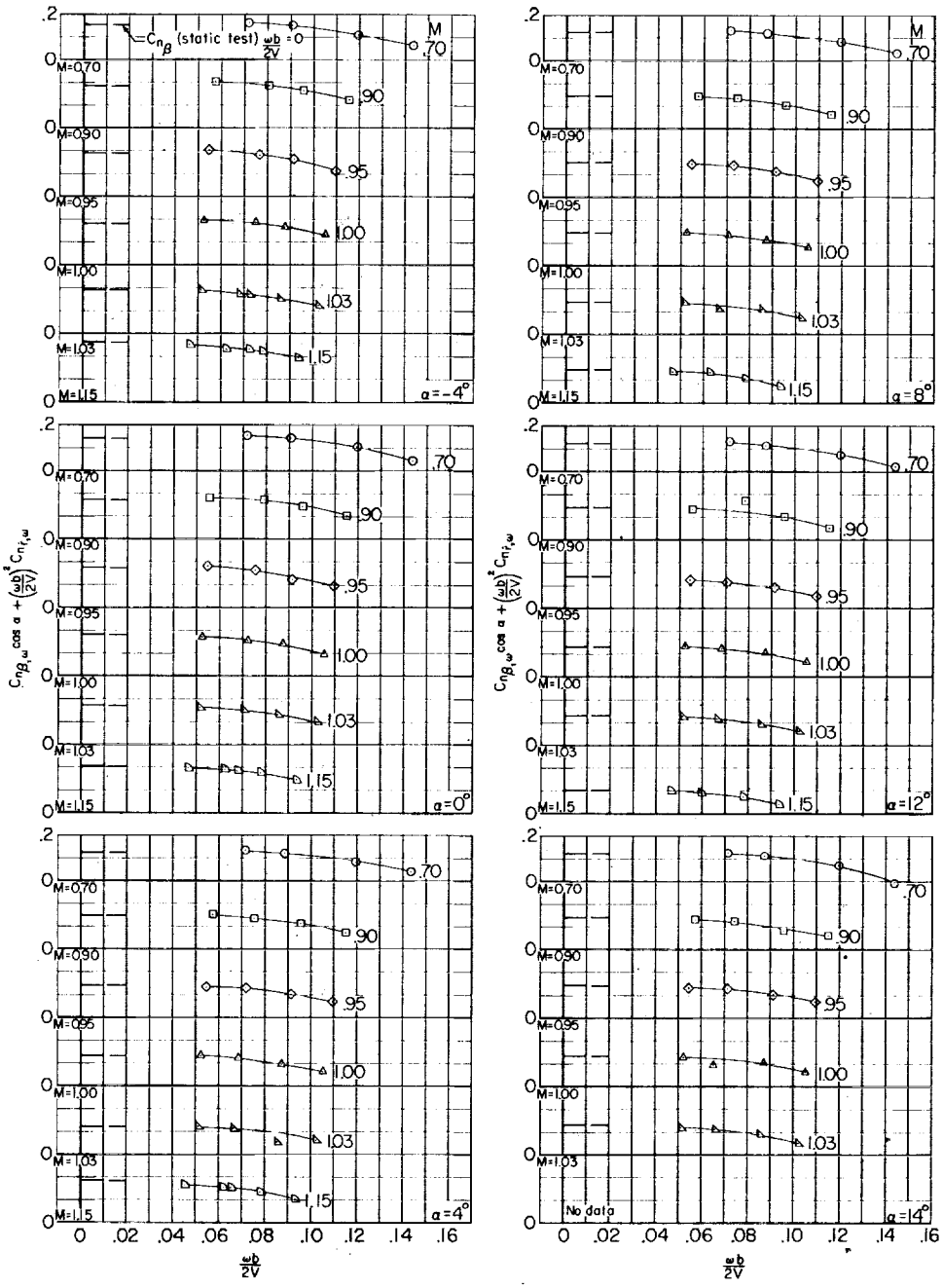

Figure 30.- Variation of oscillatory directional stability derivative $C_{n_{\beta,\omega}} \cos \alpha + \left(\frac{\omega b}{2V}\right)^2 C_{n_{\dot{r},\omega}}$ with reduced-frequency parameter $\omega b/2V$ for configuration having a body, horizontal tail, and vertical tail.

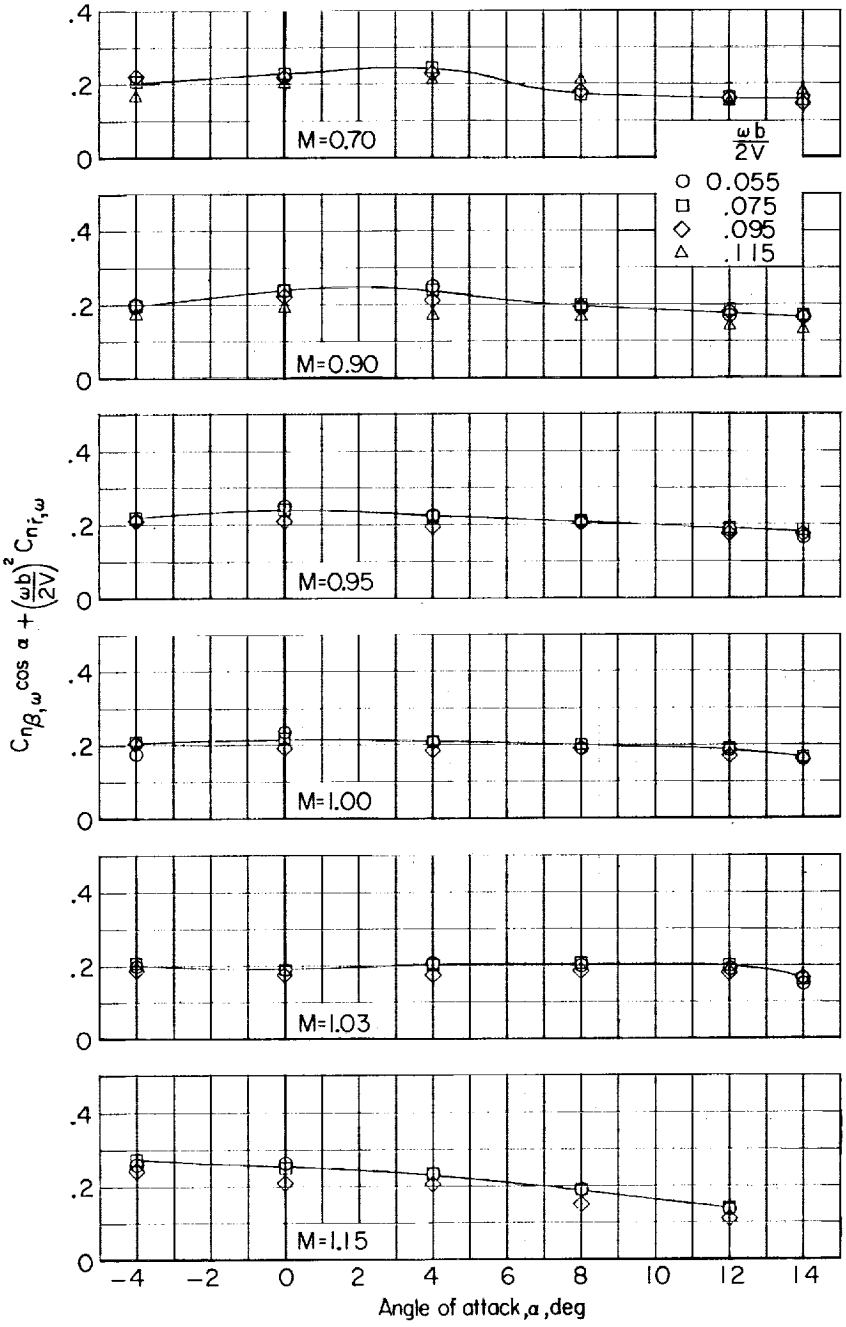

Figure 31.- Variation of $C_{n_{\beta,\omega}} \cos \alpha + \left(\frac{\omega b}{2V}\right)^2 C_{n_{\dot{r},\omega}}$ with angle of attack α for various Mach numbers for complete model.

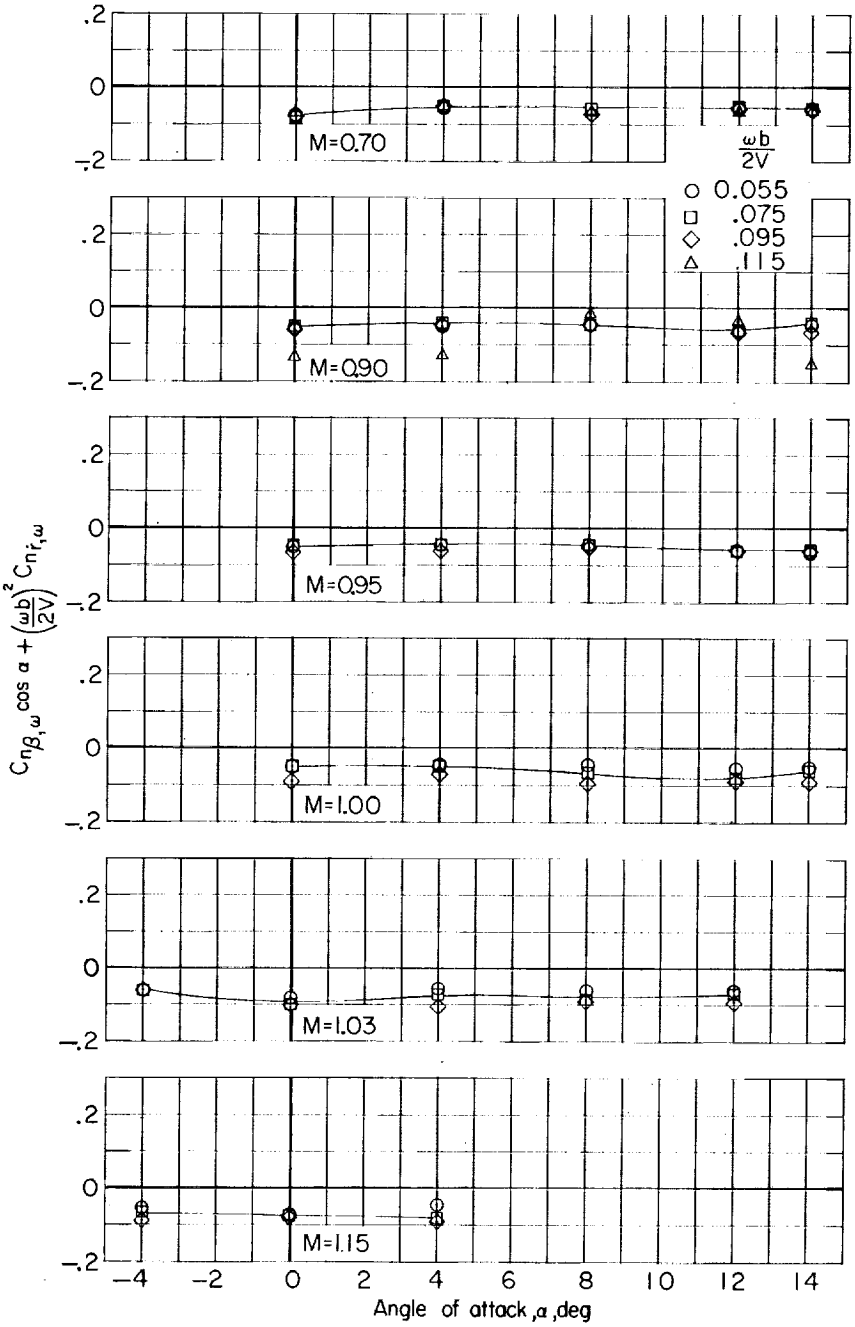

Figure 32.- Variation of $C_{n_{\beta,\omega}} \cos \alpha + \left(\frac{\omega b}{2V}\right)^2 C_{n_{\dot{r},\omega}}$ with angle of attack α for various Mach numbers for wing-body—horizontal-tail configuration.

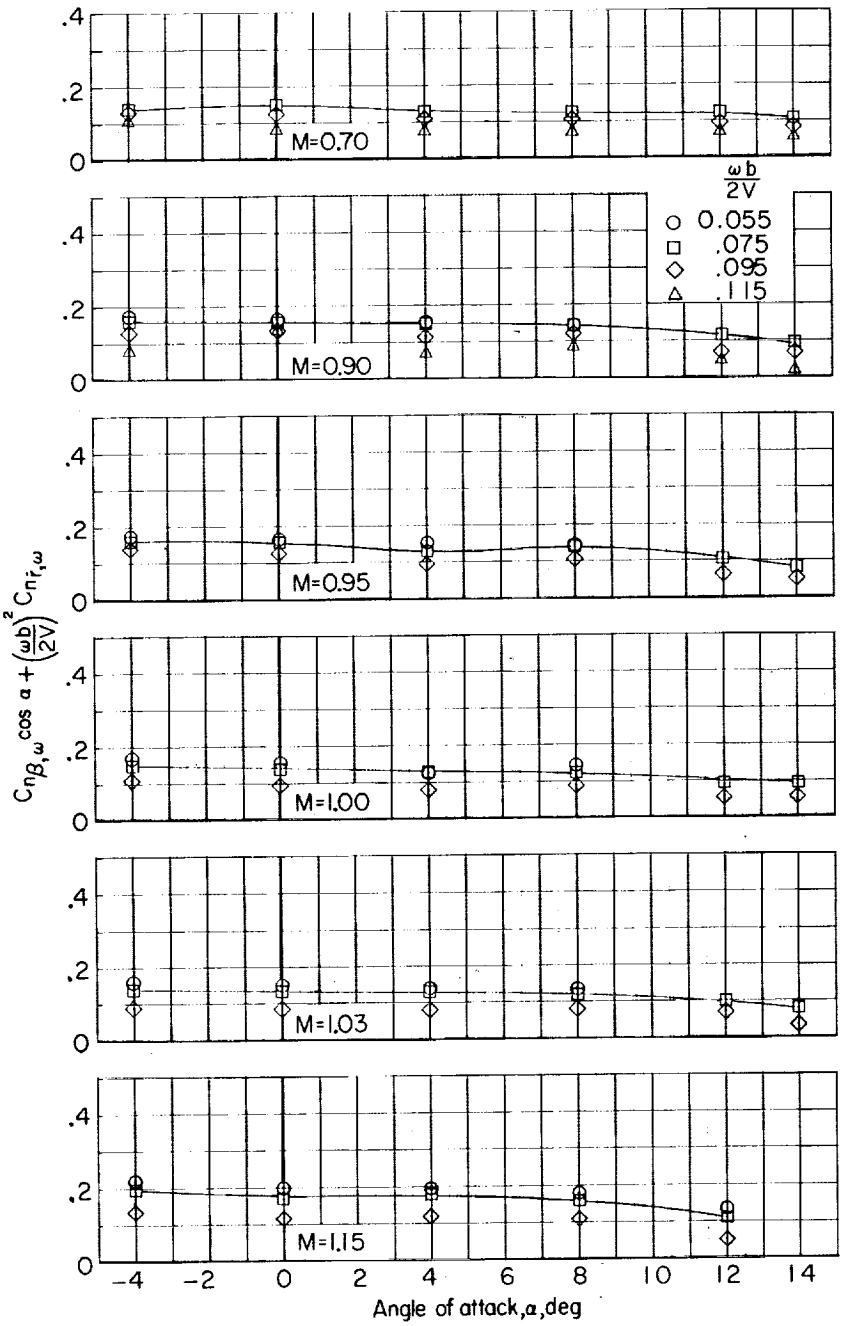

Figure 33.- Variation of $C_{n_{\beta,\omega}} \cos \alpha + \left(\frac{\omega b}{2V}\right)^2 C_{n_{\dot{r},\omega}}$ with angle of attack α for various Mach numbers for wing-body—vertical-tail configuration.

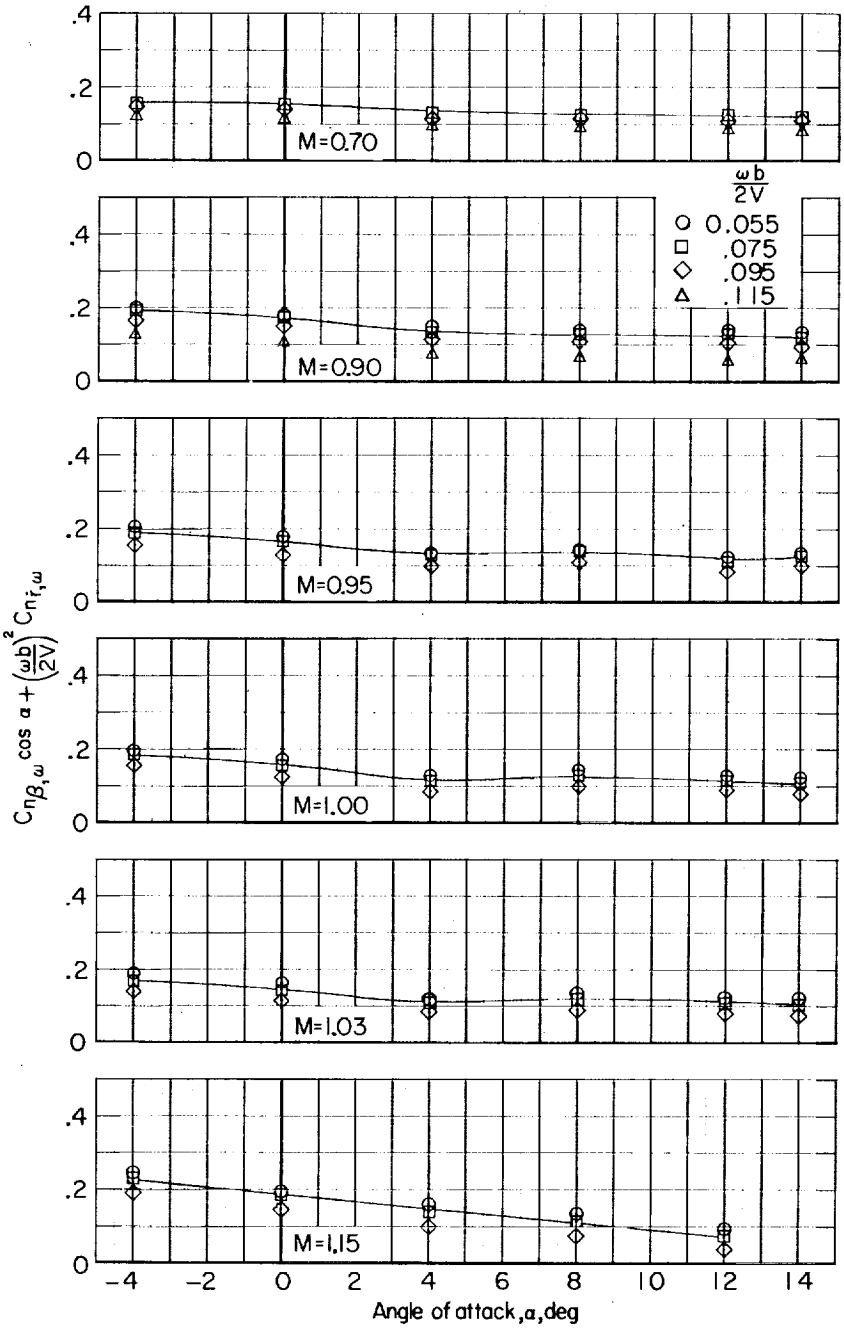

Figure 34.- Variation of $C_{n_{\beta,\omega}} \cos \alpha + \left(\frac{\omega b}{2V}\right)^2 C_{n_{\dot{r},\omega}}$ with angle of attack α for various Mach numbers for configuration having a body, horizontal tail, and vertical tail.

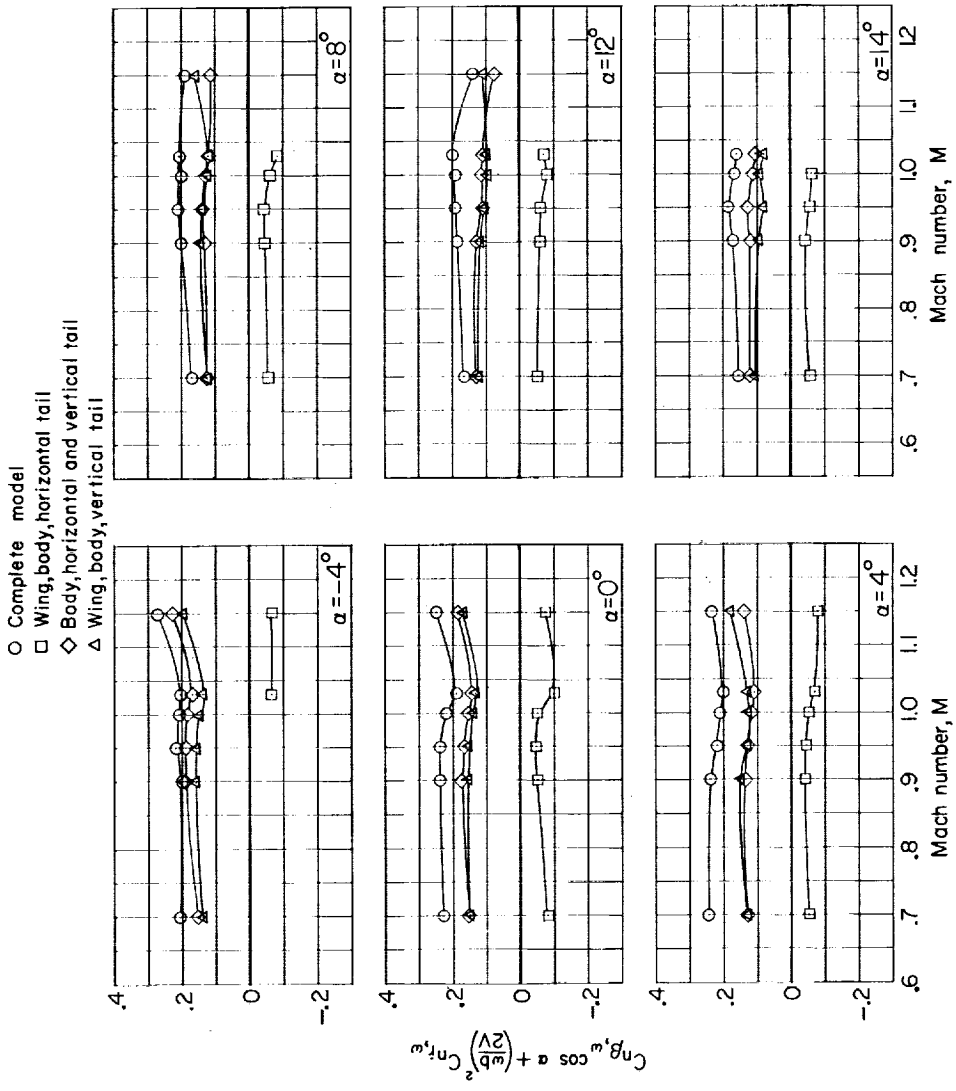

Figure 35.- Variation of $C_{n_{\beta,\omega}}\cos\alpha+\left(\frac{\omega b}{2V}\right)^2 C_{n_{r,\omega}}$ with Mach number M for various model configurations. $\omega b/2V = 0.075$.